



HAL
open science

Multiwavelength photometric study of RR lyrae variables in the globular cluster NGC 5272 (Messier 3)

Nitesh Kumar, Anupam Bhardwaj, Harinder P. Singh, Marina Rejkuba,
Marcella Marconi, Philippe Prugniel

► **To cite this version:**

Nitesh Kumar, Anupam Bhardwaj, Harinder P. Singh, Marina Rejkuba, Marcella Marconi, et al.. Multiwavelength photometric study of RR lyrae variables in the globular cluster NGC 5272 (Messier 3). *Monthly Notices of the Royal Astronomical Society*, 2024, 531, pp.2976-2997. 10.1093/mnras/stae1334 . insu-04838860

HAL Id: insu-04838860

<https://insu.hal.science/insu-04838860v1>

Submitted on 15 Dec 2024



HAL is a multi-disciplinary open access archive for the deposit and dissemination of scientific research documents, whether they are published or not. The documents may come from teaching and research institutions in France or abroad, or from public or private research centers.

L'archive ouverte pluridisciplinaire **HAL**, est destinée au dépôt et à la diffusion de documents scientifiques de niveau recherche, publiés ou non, émanant des établissements d'enseignement et de recherche français ou étrangers, des laboratoires publics ou privés.



Distributed under a Creative Commons Attribution 4.0 International License

Multiwavelength photometric study of RR Lyrae variables in the globular cluster NGC 5272 (Messier 3)

Nitesh Kumar ¹★, Anupam Bhardwaj ², Harinder P. Singh,¹ Marina Rejkuba,³ Marcella Marconi ⁴ and Philippe Prugniel⁵

¹Department of Physics and Astrophysics, University of Delhi, Delhi 110007, India

²Inter University Center for Astronomy and Astrophysics (IUCAA), Post Bag 4, Ganeshkhind, Pune 411007, India

³European Southern Observatory, Karl-Schwarzschild Strasse 2, D-85748 Garching, Germany

⁴INAF – Osservatorio Astronomico di Capodimonte, Salita Moiariello 16, I-80131 Naples, Italy

⁵Université de Lyon, Université Lyon 1, 69622 Villeurbanne; CRAL, Observatoire de Lyon, CNRS UMR 5574, F-69561 Saint-Genis Laval, France

Accepted 2024 May 19. Received 2024 May 14; in original form 2023 September 20

ABSTRACT

We present a comprehensive photometric study of RR Lyrae stars in the M3 globular cluster, utilizing a vast data set of 3140 optical (*UBVRI*) CCD images spanning 35 yr from astronomical data archives. We have successfully identified previously known 238 RR Lyrae stars from the photometric data, comprising 178 RRab, 49 RRc, and 11 RRd stars. Multiband periodogram was used to significantly improve the long-term periods of 65 per cent of RR Lyrae stars in our sample, thanks to the unprecedentedly long temporal coverage of the observations. The light curve templates were used to obtain accurate and precise mean magnitudes and amplitudes of all RR Lyrae variables. We combined optical (*UBVRI*) and near-infrared (NIR, *JHK_s*) photometry of RR Lyrae variables to investigate their location in the colour-magnitude diagrams as well as the pulsation properties such as period distributions, Bailey diagrams and amplitude ratios. The period–luminosity relations in *R* and *I* bands and Period–Wesenheit relations were derived after excluding outliers identified in CMDs. The Period–Wesenheit relations calibrated via the theoretically predicted relations were used to determine a distance modulus of $\mu = 15.04 \pm 0.04$ (stats) ± 0.19 (syst.) mag (using metal-independent W_{BV} Wesenheit) and $\mu = 15.03 \pm 0.04$ (stats) ± 0.17 (syst.) mag (using metal-dependent W_{VI} Wesenheit). Our distance measurements are in excellent agreement with published distances to M3 in the literature. We also employed an artificial neural network based comparison of theoretical and observed light curves to determine physical parameters (mass, luminosity, and effective temperature) for 79 non-Blazhko RRab stars that agree with limited literature measurements.

Key words: methods: data analysis – techniques: photometric – stars: variables: RR Lyrae.

1 INTRODUCTION

RR Lyrae stars are low mass ($0.5 \lesssim M/M_{\odot} \lesssim 0.8$), evolved stars (age $\gtrsim 10$ Gyr, Savino et al. 2020) located at the intersection of the horizontal branch and classical *instability strip* in the Hertzsprung–Russell diagram. They are in their central helium-burning phase of the evolutionary stage, similar to the intermediate-mass classical Cepheids ($3 \lesssim M/M_{\odot} \lesssim 13$). Due to their well-defined period–luminosity relations (PLRs) at infrared wavelengths, first discussed by Longmore, Fernley & Jameson (1986) and later studied by many others, including Bono et al. (2001); Catelan, Pritzl & Smith (2004); Sollima, Cacciari & Valenti (2006); Muraveva et al. (2015); Bhardwaj et al. (2021), RR Lyrae variables are useful for deriving distances and potentially calibrating the first step of the cosmic distance ladder (Beaton et al. 2016; Bhardwaj 2020). Additionally, they are valuable for studying stellar evolution and pulsation (Catelan 2009), as well

as for tracing old stellar populations in their host galaxies (Kunder et al. 2018).

NGC 5272 (also known as Messier 3 or M3, with R.A. (J2000) = $13^{\text{h}}42^{\text{m}}11^{\text{s}}$ and Dec (J2000) = $+28^{\circ}22'32''$) is a globular cluster located approximately 11.9 kpc from the Galactic Centre, about 10 kpc from the Sun, and around 9.7 kpc above the Galactic plane (Harris 1996). This cluster has a population of approximately 240 RR Lyrae stars, many of which are fundamental mode RR Lyrae (RRab) stars (Clement et al. 2001). M3 is considered a mono-metallic cluster with a mean metallicity of $[\text{Fe}/\text{H}] \sim -1.5$ dex (Harris 2010). The period distribution of the RR Lyrae population in M3 shows a sharp peak at a fundamental pulsation period of ~ 0.55 d (Jurcsik et al. 2017), classifying this cluster as a typical Oosterhoff I (OoI) type cluster (Oosterhoff 1939; Fabrizio et al. 2019).

The large population of RR Lyrae stars and a proximity to M3 have already motivated several long-term studies of optical photometric monitoring (Kaluzny et al. 1997; Corwin & Carney 2001; Clementini et al. 2003; Hartman et al. 2005; Benkő, Bakos & Nuspl 2006; Jurcsik et al. 2012, 2015, 2017), as well as several spectroscopic investigations (Snedden et al. 2004; Cohen & Meléndez

* E-mail: niteshchandra039@gmail.com

2005; Johnson et al. 2005; Givens & Pilachowski 2016). Siegel et al. (2015) investigated the RR Lyrae population of M3 at ultraviolet wavelengths. Longmore et al. (1990) first carried out near-infrared (NIR) studies of RR Lyrae stars in M3 and derived PLR in the K_s -band using 49 variables from the outer region of the cluster. A more recent investigation by Bhardwaj et al. (2020) presented a time-series analysis that included PLRs derived from 233 RR Lyrae stars in M3, observed in the J , H , and K_s bands.

Several theoretical studies have focused on M3 variables, aiming to reproduce their observed pulsation properties, focusing on the period distribution of the RR Lyrae population. These studies were carried out by Marconi et al. (2003), Catelan (2004b), Castellani, Castellani & Cassisi (2005), and Fadeyev (2019). The study conducted by Catelan (2004b) demonstrated that the predicted period distribution, based on canonical horizontal branch models, does not align with observations. In contrast, Castellani et al. (2005) suggested that a bimodal mass distribution would be necessary to replicate the observed period distribution using canonical models. Denissenkov et al. (2017) used horizontal branch models to investigate the properties of RR Lyrae and non-variable horizontal branch stars in M3. They found that a distance modulus of $\mu = 15.02$ mag and a reddening value of $E(B - V) = 0.013$ mag provided good agreement with the observed properties of these stars. Utilizing the full-phased light curves of RR Lyrae stars, Marconi & Degl’Innocenti (2007) employed non-linear pulsation models to accurately simulate the optical light curves constraining physical parameters of RR Lyrae stars in M3.

While M3 has been extensively studied in the past at optical wavelengths, most studies had limited temporal baseline and wavelength coverage in BVI bands (Corwin & Carney 2001; Cacciari, Corwin & Carney 2005; Hartman et al. 2005; Benkő et al. 2006; Jurcsik et al. 2012, 2017, and references therein). At longer wavelengths, Bhardwaj et al. (2020) provided homogeneous NIR photometry of RR Lyrae variables in M3. A multiband photometric study of the large sample of RR Lyrae in M3 using a vast data set covering long time-baseline and spectral-coverage of observations will be useful to explore and analyse the pulsation properties of RR Lyrae stars in unprecedented detail. Homogeneous optical and NIR light curves will also be useful in modelling multiband light curves, constraining input parameters to stellar pulsation models. In particular, the optical photometry together with NIR photometric mean magnitudes adopted from Bhardwaj et al. (2020) will be useful in deriving multiband PLRs and optical-NIR PWRs for RR Lyrae based distance measurements. Moreover, the light curves of a considerable proportion of RR Lyrae stars exhibit amplitude and phase modulations over a time-scale significantly longer than their primary pulsation period (e.g. in M3 RR Lyrae in Jurcsik et al. 2018). This phenomenon is commonly referred to as the Blazhko effect (Blazhko 1907; Shapley 1916). Despite being discovered nearly a century ago, the root cause of this phenomenon is not known, emphasizing the need for further investigation using long-term ground and space-based photometric data (Molnár et al. 2021).

The structure of the current paper is as follows: In Section 2, we present the optical photometric observations in various standard filter bands. The identification, period determination, template fitting methodology, and period amplitude diagrams are discussed in Section 3. The colour-magnitude diagrams (CMD) of stars in M3 are presented in Section 3.4. Empirical period luminosity (PL) and Period–Wesenheit (PW) relations are derived in Section 4, including a determination of the distance to M3. Fourier parameters of RR Lyrae stars of M3 in different optical bands are obtained and discussed in Section 5.1, and the physical parameters of non-

Blazhko RRab stars are derived using an artificial neural network (ANN), as described in Section 5.2. Finally, we summarize our work in Section 6.

2 OPTICAL PHOTOMETRY

We provide accurate, homogeneous, and consistently calibrated multiband $UBVRI$ photometry for the candidate RR Lyrae stars in M3 based on 3140 optical CCD images obtained from public archives. The observational log and the details of different optical data sets employed in this study are provided in Table 1. The interested readers are referred to Stetson et al. (2019) for details regarding homogeneous photometry of globular clusters using archival imaging data sets.

All images were preprocessed in a standard way, including bias subtraction and flat-fielding. The photometry and calibration were carried out using the DAOPHOT/ALLFRAME software suite (Stetson 1987, 1994). Following the detection of sources and determination of the PSFs in each image, geometric and photometric information for all detected objects was used to derive a self-consistent set of positions and magnitudes for all stars in every image. This is similar to procedures used in the study of Messier 4, and we refer to Stetson et al. (2014b) for more details. We note that the data sets from different telescopes and instruments on different photometric nights were calibrated with respect to standard stars in many different fields, also including atmospheric extinction corrections. The observations that were taken in non-photometric conditions were calibrated with local secondary standards within the images, which themselves were calibrated with the standard stars. All the possible systematic uncertainties were propagated to the photometric measurements, and therefore, these observations are reliably homogenized within their quoted uncertainties.

The calibrated photometry covers a sky area of approximately 57×56 arcmin, enclosing the cluster centre. A total of 3140 images were successfully photometrically calibrated, including 228 U -band, 1108 B -band, 1215 V -band, 198 R -band, and 391 I -band images, spanning slightly over 35 yr. The optical time-series photometry of RR Lyrae stars of M3 is provided in Table 2. We have a maximum of 64/277/299/40/96 observations and a minimum of 2/18/16/4/2 observations in $UBVRI$ bands, respectively. The median number of observations in $U/B/V/R/I$ filters are 58/249/264/27/66.

Our sample had several photometric measurements in different standard filters (such as Sloan u , g , r , i , and Stroemgren b , y filters), which were transformed to standard Johnson/Kron–Cousins photometric $UBVRI$ bands defined by the equatorial standards of Landolt (1992). While these measurements were valuable for period determination, we will not incorporate them for determining mean magnitudes and amplitudes. This is because their amplitudes are unreliable due to errors introduced during their photometric transformations. These filters do not precisely align with the bandpasses of standard Landolt filters and, as a result, can bias the mean magnitudes and amplitudes when performing template fitting.

3 RR LYRAE STARS IN MESSIER 3

3.1 Identification of variable stars

The identification of RR Lyrae stars in the M3 globular cluster was accomplished using the reference list compiled by Clement et al. (2001, hereafter CC01, last updated in March 2019). This list provided essential information, including coordinates, V -band amplitudes, periods, and classifications for most stars. Out of 178

Table 1. Log of the observations of M3 in optical bands. Here, the ‘Run’ column shows unique run labels, ‘Dates’ indicates the observing dates included, and n_X represents the number of images in filter X . These filters consist of the standard Landolt filters (U, B, V, R, I), Sloan filters (u, g, r, i), and Stromgren filters (u, b, y). The ‘Multiplex’ column denotes the number of CCDs in mosaic cameras.

No.	Run	Dates	Telescope	Camera	n_U, n_B, n_V, n_R, n_I	n_u, n_b, n_y	n_u, n_g, n_r, n_i	Multiplex
1	cf84	1984 Jun 22	Maunakea CFHT 3.6-m	RCA1	-, 1, 1, -, -	-, -, -	-, -, -, -	-
2	kp36	1985 Jun 12	KPNO 0.9-m	RCA	-, 4, 4, -, -	-, -, -	-, -, -, -	-
3	kp4m	1985 Jun 16–18	KPNO 4-m	RCA	-, 6, 5, -, -	-, -, -	-, -, -, -	-
4	cf85	1985 Jun 20–24	Maunakea CFHT 3.6-m	RCA1	-, 10, 10, -, -	-, -, -	-, -, -, -	-
5	jvw	1986 Mar 29-Apr 09	La Palma INT 2.5-m	RCA	4, 6, 8, 9, 6	-, -, -	-, -, -, -	-
6	km	1986 May 08	La Palma INT 2.5-m	RCA	-, 1, 2, -, -	-, -, -	-, -, -, -	-
7	c91ic41	1991 Apr 08	Maunakea CFHT 3.6-m	lick1	-, 2, 2, -, 2	-, -, -	-, -, -, -	-
8	cf91	1991 Jul 06–07	Maunakea CFHT 3.6-m	Lick2	-, 2, 2, -, -	-, -, -	-, -, -, -	-
9	saic	1992 May 25	Maunakea CFHT 3.6-m	HRCam/saic1	-, -, 16, 15, -	-, -, -	-, -, -, -	-
10	h92ic1	1992 May 27	Maunakea CFHT 3.6-m	HRCam	-, 7, -, -, -	-, -, -	-, -, -, -	-
11	cf92	1992 Jun 08–09	Maunakea CFHT 3.6-m	RCA4	-, 3, -, -, -	-, -, -	-, -, -, -	-
12	bolte	1994 Apr 13–16	KPNO 2.1-m	t1ka	-, -, 30, -, 31	-, -, -	-, -, -, -	-
13	cf94	1994 Jun 06	Maunakea CFHT 3.6-m	Loral3	-, 4, -, -, 4	-, -, -	-, -, -, -	-
14	jka	1995 Mar 27	La Palma INT 2.5-m	TEK3	-, 3, 8, -, -	-, -, -	-, -, -, -	-
15	bond9	1997 May 08–10	KPNO 0.9-m	t2ka	-, 4, 4, -, 4	-, -, -	4, -, -, -	-
16	arg	1997 May 31	La Palma JKT 1-m	TEK2	-, -, 3, -, 6	-, -, -	-, -, -, -	-
17	bond11	1998 Mar 21–22	KPNO 0.9-m	t2ka	-, 9, 9, -, 9	-, -, -	1, -, -, -	-
18	int9804	1998 Apr 12	La Palma INT 2.5-m	WFC	-, 3, -, 4, -	-, -, -	-, -, -, -	-
19	dmd	1998 Jun 24	La Palma JKT 1-m	TEK4	-, -, 2, -, 2	-, -, -	-, -, -, -	-
20	tng2	2000 Feb 04	La Palma TNG 3.6-m	OIG	2, 2, 2, -, -	-, -, -	-, -, -, -	x 2
21	int0005	2000 May 24–28	La Palma INT 2.5-m	WFC	-, 3, 3, -, -	-, -, -	-, -, -, -	x 4
22	jun00	2000 Jun 04	Maunakea CFHT 3.6-m	CFH12K	-, -, 2, -, -	-, -, -	-, -, -, -	x 12
23	cf0102	2001 Feb 16–17	Maunakea CFHT 3.6-m	CFH12K	-, 15, 18, -, 12	-, -, -	-, -, -, -	x 12
24	not017	2001 Jul 11–15	La Palma NOT 2.6-m	CCD7	-, 9, 7, -, 10	-, -, -	-, -, -, -	-
25	int0202	2002 Feb 03–04	La Palma INT 2.5-m	WFC	-, 112, 113, -, -	-, -, -	-, -, -, -	x 4
26	hannah	2002 Mar 29	La Palma JKT 1-m	SIT2	-, 5, 11, 10, -	-, -, -	-, -, -, -	-
27	int1005	2010 May 25–30	La Palma INT 2.5-m	WFC	-, 32, 33, 33, 11	-, -, -	-, -, -, -	x 4
28	lee3	2011 May 24–27	KPNO 4-m	Mosaic1.1	-, -, -, -, -	-, 18, 17	-, -, -, -	x 8
29	int1202	2012 Feb 22–23	La Palma INT 2.5-m	WFC	16, -, -, -, -	-, -, -	-, -, -, -	x 4
30	int1204	2012 Apr 23–26	La Palma INT 2.5-m	WFC	10, 9, 9, -, 6	-, -, -	-, -, -, -	x 4
31	int1304	2013 Apr 13	La Palma INT 2.5-m	WFC	10, -, -, -, -	-, -, -	-, -, -, -	x 4
32	spm1405a	2014 May 21	S Pedro Martir 0.8	E2V-4290	1, 2, 2, 2, 2	-, -, -	-, -, -, -	-
33	dahl	2014 Jun 19–25	Maria Mitchell 0.4	Roper PVCAM	-, -, 3, 3, -	-, -, -	-, -, -, -	-
34	int1501	2015 Jan 30	La Palma INT 2.5-m	WFC	-, 2, 2, -, -	-, -, -	-, -, -, -	x 4
35	int1502	2015 Feb 25–27	La Palma INT 2.5-m	WFC	-, 9, 9, -, -	-, -, -	-, -, -, -	x 4
36	int1504	2015 Apr 24–27	La Palma INT 2.5-m	WFC	-, 16, 17, -, 8	-, -, -	-, -, -, -	x 4
37	int1605	2016 May 28-Jun 02	La Palma INT 2.5-m	WFC	1, 11, 11, -, 10	-, -, -	-, -, -, -	x 4
38	int1704	2017 Apr 03–05	La Palma INT 2.5-m	WFC	-, 6, 6, -, 6	-, -, -	-, -, -, -	x 4
39	iac80a	2017 Jun 17–19	Teide IAC80 0.8-m	CAMELOT	2, 2, 2, 2, 2	-, -, -	-, -, -, -	-
40	spm1801b	2018 Jan 28	S Pedro Martir 0.8	E2V-4240	2, 2, 2, 2, 2	-, -, -	-, -, -, -	-
41	int1802	2018 Feb 22	La Palma INT 2.5-m	WFC	3, 3, -, -, -	-, -, -	-, -, -, -	x 4
42	spm1802	2018 Feb 26	S Pedro Martir 2.1	E2V-4240	3, 3, 2, 3, 3	-, -, -	-, -, -, -	-
43	int1805	2018 May 20–22	La Palma INT 2.5-m	WFC	6, 2, 6, 2, -	-, -, -	-, -, -, -	x 4
44	int1806	2018 Jun 12	La Palma INT 2.5-m	WFC	2, 2, -, 2, -	-, -, -	-, -, -, -	x 4
45	int1906	2019 Jun 26–29	La Palma INT 2.5-m	WFC	5, 2, -, -, -	-, -, -	-, -, -, -	x 4

Notes. 1. Observers R. D. McClure and D. A. VandenBerg, 2. Observer P. B. Stetson, 3. Observer P. B. Stetson, 4. Observers J. E. Hesser and D. A. VandenBerg, 5. Observer ‘JVW’, 6. Observer ‘KM’, 7. Observers H. Richer and G. Fahlman, 8. Observers P. B. Stetson and J. E. Hesser, 9. Observers Bolte and Hesser, 10. Observers Richer and Buonanno, 11. Observers P. B. Stetson and M. Bolte, 12. Observer M. Bolte, 13. Run ID 94IC15, observers D. A. VandenBerg and P. B. Stetson, 14. Observer ‘JKA’, 15. Proposal KP2771, observer H. E. Bond; includes observations in Sloan u filter, 16. Observer A. Rosenberg, 17. Proposal 98A-0351, observer H. E. Bond, 18. Details unavailable, 19. Run number 4064, observer ‘DMD’, 20. Observers Ortolani, Bragaglia and ‘admin’, 21. Proposal P14, observer Robert Greimel, 22. Run ID 00AC14, observers Stetson and Fahlman, 23. Run IDs 01AK1 and 01AF43, observers Park, Sohn and Oh; R. Ibata and C. Pichon, 24. Observer Bruntt, 25. Proposal P20, observer G. Gilmore, 26. Proposal ‘ING_Science,’ observer Javier Mendez, 27. Proposal N5, observer vdWerf, 28. Proposal ID 2011A-0197, observer J.-W. Lee, 29. Proposal C34, observer Carrera, 30. Proposal c70, observer Milone, 31. Proposal C143, observer M. Monelli, 32. Observers Ricci et al. and Ayala-Michel; data contributed by Raul Michel Murillo, 33. Observer E. Dahl, 34. Proposals CAT.S and N22W, observers Oscoz and Vats, 35. Proposal C115, observer C. Martinez, 36. Proposal N2, observer Henk Hoekstra; proposal C115, observer Clara Martinez, 37. Proposal C143, observer Monelli, 38. Proposals ‘(16A)C143’ and ‘CAT.S,’ observer M. Monelli, 39. Observer M. Monelli, 40. Observers Omar and Raul; data contributed by Raul Michel Murillo, 41. Proposal C14, observer M. Monelli, 42. Observers ‘ing’ and Michel; data contributed by Raul Michel Murillo, 43. Proposal C14, observer M. Monelli, 44. Proposal C14, observers Monelli and Rusakov, and 45. Proposal C143, observer Monelli.

Table 2. Optical time-series photometry of RR Lyrae stars in M3 cluster. The complete table can be accessed online in machine-readable format.

Id	Run name	Image name	Band	Filter flag	HJD	mag	σ_{mag}	χ	Sharp
V1	bond9	obj1801	<i>U</i>	b	2450576.8756	15.835	0.0446	1.55	0.056
V1	bond9	obj3001	<i>U</i>	b	2450577.8346	15.320	0.0199	1.66	0.010
V1	bond9	obj4201	<i>U</i>	b	2450578.8378	16.346	0.0347	2.26	0.106
V1	bond9	obj4205	<i>U</i>	b	2450578.8563	15.673	0.0256	2.23	0.067
V1	bond11	obj6801	<i>U</i>	b	2450894.9046	15.370	0.0215	1.58	0.036
V1	int1202	1m3U30a_4	<i>U</i>	a	2455979.6201	15.689	0.0136	1.52	0.170
⋮	⋮	⋮	⋮	⋮	⋮	⋮	⋮	⋮	⋮
V1	c91ic41	111709o	<i>B</i>	a	2448354.9710	15.568	0.0191	4.40	0.229
V1	c91ic41	111710o	<i>B</i>	a	2448354.9777	15.611	0.0118	5.14	0.069
V1	bond9	obj1802	<i>B</i>	a	2450576.8794	15.628	0.0317	1.93	0.103
⋮	⋮	⋮	⋮	⋮	⋮	⋮	⋮	⋮	⋮
V1	c91ic41	111716o	<i>V</i>	a	2448354.9901	15.413	0.0254	5.33	0.106
V1	c91ic41	111718o	<i>V</i>	a	2448354.9972	15.457	0.0162	7.93	−0.026
V1	bond9	obj1803	<i>V</i>	a	2450576.8815	15.390	0.0257	1.64	0.106
⋮	⋮	⋮	⋮	⋮	⋮	⋮	⋮	⋮	⋮
V1	c91ic41	111693o	<i>I</i>	a	2448354.9374	14.876	0.0185	4.87	−0.060
V1	c91ic41	111694o	<i>I</i>	a	2448354.9464	14.896	0.0239	11.47	−0.009
V1	bond9	obj1804	<i>I</i>	a	2450576.8836	15.024	0.0326	2.12	0.111
⋮	⋮	⋮	⋮	⋮	⋮	⋮	⋮	⋮	⋮
V1	int1805	r1388819_4	<i>R</i>	a	2458261.4427	15.527	0.0108	4.12	0.488
V1	int1806	r1392560_4	<i>R</i>	a	2458282.4129	15.652	0.0095	1.55	0.556
V1	int1806	r1392561_4	<i>R</i>	a	2458282.4145	15.647	0.0114	3.08	0.636
V3	bond9	obj1801	<i>U</i>	b	2450576.8756	15.102	0.0264	1.37	0.026
V3	bond9	obj3001	<i>U</i>	b	2450577.8346	16.391	0.0352	1.49	0.081
V3	bond9	obj4201	<i>U</i>	b	2450578.8378	16.323	0.0333	2.09	0.093
V3	bond9	obj4205	<i>U</i>	b	2450578.8563	16.364	0.0269	1.53	0.081
V3	bond11	obj6801	<i>U</i>	b	2450894.9046	16.384	0.0366	1.42	0.014
V3	int1202	1m3U30a_4	<i>U</i>	a	2455979.6201	15.930	0.0122	1.16	0.164
⋮	⋮	⋮	⋮	⋮	⋮	⋮	⋮	⋮	⋮

Note. The identifier (Id) corresponds to the nomenclature used in the catalogue by Clement et al. (2001). HJD denotes the Heliocentric Julian Date. Image quality indices χ and Sharp pertain to the original image. The filter flag ‘a’ signifies observations conducted with the ‘Landolt’ filter, ‘b’ indicates observations initially in the ‘Sloan’ filter and later transformed to Landolt, while ‘c’ denotes observations in the ‘Stromgren’ filter converted to Landolt. We note that these transformed Landolt magnitudes are marked with different symbols in the light curves presented in the manuscript.

RRab stars classified in CC01, 176 stars were present in our sample, with data missing for V206 and V4s stars. V217 was identified as an RRab star by Siegel et al. (2015) and V265 was identified as an RRab star by Bhardwaj et al. (2020), both of which were subsequently adopted in our analysis bringing the total number of RRab stars to 178. We extracted 49 RRc stars reported by CC01; however, a few of them had to be removed due to data quality concerns (see Section 3.4). Moreover, there are 11 double/multimode (RRd) variables in our sample, making the total number of RR Lyrae stars 238. The Oosterhoff classification and Blazhko type for these stars were adopted following Jurcsik et al. (2015, 2017). Among the analysed stars, 90 were Blazhko variables, with 81 RRab, 5 RRc, and 4 RRd type stars being part of this group.

3.2 Period determination and distribution

To test the accuracy of literature periods, we re-determined periods of RR Lyrae stars based on our long temporal baseline data available in multiple bands. In our analysis, we utilized the Multiband Lomb–Scargle (MBLS) algorithm (VanderPlas & Ivezić 2015), a modified version of the traditional Lomb–Scargle (LS) algorithm (Lomb 1976; Scargle 1982). The MBLS algorithm is designed to handle photometric time-series data available in multiple bands.

In the classical LS algorithm, a Fourier transform is performed, generating a power spectrum with candidate frequencies (periodogram). The frequency with the highest power corresponds to the period of the given time-series data. The MBLS algorithm, on the other hand, models the light curves in each band as a Fourier series truncated to arbitrary terms that share the same period and phase among all filter pass bands. This common base model is used across all bands. Subsequently, individual fits are made, and residuals relative to the base model are calculated, resulting in a combined high-power frequency periodogram that considers all bands together, corresponding to the fundamental period.

The PYTHON module Gatspy¹ offers an implementation of the MBLS algorithm for period determination. The typical error bar in the derived periods is 10^{-6} d (determined by Monte-Carlo simulation using PERIOD04, Lenz & Breger 2005). Using the MBLS algorithm, we determined periods for 238 RR Lyrae stars. RR Lyrae stars are known to exhibit both monotonic and random period changes with a typical mean period change rate of the order of 0.01 d Myr^{-1} (Szeidl et al. 2011; Jurcsik et al. 2012; Li, Qian & Zhu 2018). This suggests that a period change of approximately 3.5×10^{-7} d would be expected

¹<https://github.com/astroML/gatspy>

over a 35-yr baseline. The sparseness of our light curve sampling results in typical uncertainties of 10^{-6} d in periods and is not ideal for the study of period changes. To assess the consistency, validity, and accuracy of the derived periods, we performed phase-folding on the light curves using periods obtained through the MBLs method and those reported by Jurcsik et al. (2015, 2017), Jurcsik (2019), Bhardwaj et al. (2020), and Clement et al. (2001). Subsequently, we calculated the *string length* per unit phase. Notably, among the 238 RR Lyrae stars, the MBLs-derived periods exhibited the lowest string length per unit phase for 154 stars. Additionally, periods for 62 RR Lyrae stars were adopted from Jurcsik et al. (2015, 2017) and Jurcsik (2019), as they showed the lower string length per unit phase. Furthermore, periods for 21 stars were adopted from Clement et al. (2001) based on the same criterion, and the period for one RR Lyrae star (V265) was sourced from Bhardwaj et al. (2020).

A comparison of the phase-folded light curves of stars V17 and V129 with different periods is shown in Fig. 1. For V17, the change in period is 0.000033 d when compared with the period derived by Jurcsik (2019). It is evident that the observed period derived using MBLs is more accurate for both V17 and V129, as the folded light curve has a lower string length and less scatter.

Fig. 2 shows the comparison of the periods of RR Lyrae stars derived using MBLs and the published periods in the literature (Jurcsik et al. 2015, 2017; Jurcsik 2019). We note that periods determined in these literature studies are based on dedicated time-series photometry of M3, with well-sampled light curves, but within a much smaller time-baseline than this work. We notice an excellent agreement with the literature periods, where in most cases our derived periods improved the phase light curves based on long-term data. Literature periods were adopted where periods were not determined accurately in our sample. The derived period will be useful for O-C analysis to study the long-term period changes of the RR Lyrae stars in M3 (e.g. Jurcsik et al. 2012; Li et al. 2018).

The period distribution of RR Lyrae stars is displayed in Fig. 3. RRab stars exhibit a wide range of periods, from approximately 0.45 to 0.8 d. However, we do not observe any long-period RR Lyrae stars ($P \geq 0.82$ d) as they are relatively rare in Galactic globular clusters, with only a few instances found in metal-rich globular clusters such as NGC 6388 and NGC 6441 (Pritzl et al. 2001, 2002; Bhardwaj 2022), as well as in the Galactic field (Wallerstein, Kovtyukh & Andrievsky 2009).

For typical Oosterhoff I clusters, the ratio between the number of RRc (N_c) and the total number of RR Lyrae stars ($N_{\text{tot}} = N_{\text{ab}} + N_c + N_d$) is approximately 0.29. In contrast, it is around 0.44 for OoII clusters (Oosterhoff 1939; Castellani & Quarta 1987; Caputo 1990). In the case of the M3 cluster, the ratio $N_c/N_{\text{tot}} \sim 0.21$ indicates consistency with an OoI-type cluster.

M3's RRab stars exhibit a mean period (0.562 d) consistent with Oosterhoff type I (OoI) clusters, while OoII clusters have longer periods, as can be seen in Fig. 3. Similarly, the mean period of M3's RRc stars (0.342 d) falls within the range of both OoI and OoII types. The mean metallicity similar to that of M3 ($[\text{Fe}/\text{H}] \sim -1.5$ dex) typically separates these two Oosterhoff type clusters (Catelan 2009).

3.3 Template fitting

The estimation of mean magnitudes for RR Lyrae stars from their sparsely sampled light curves can be achieved by fitting template light curves, requiring fundamental parameters such as period, the epoch of maximum light, and amplitude ratio. Utilizing this template fitting approach, it has been possible to achieve a precision of a few hundredths of a magnitude in estimating mean magnitudes, even

for light curves with only a few phase points (Jones, Carney & Fulbright 1996; Soszyński, Gieren & Pietrzyński 2005; Inno et al. 2015; Bhardwaj et al. 2020).

We used the templates generated by Sesar et al. (2009) using Stripe 82 SDSS data to perform a χ^2 minimization approach for fitting our observed phased light curves. The template collection consists of 11 templates in the *u*-band, 21 templates in the *g*-band, 20 templates in the *r*-band, 20 templates in the *i*-band, and 18 templates in the *z*-band for RRab stars. Similarly, for RRc stars, the template numbers are 1, 2, 2, 2, and 1 in the respective order. In our analysis, we note that *ugriz* filters are not the same as *UBVRI*, but the approximate light curve shape is not expected to vary significantly at similar wavelengths. Since the template light curves are not available in *UBVRI*, these *ugriz* templates will best determine mean magnitudes for our RR Lyrae stars. The templates in the 'g' band were employed for fitting both the *V*- and *B*-band light curves, whereas the templates in the 'u', 'r', and 'i' bands were utilized for fitting the *U*-, *R*-, and *I*-band light curves, respectively. The templates were sequentially applied to the observed phased light curve corresponding to the appropriate filter. We minimized the χ^2 deviation between the actual magnitude measurements (m) and the template fit magnitudes (m_{fit}).

We phased-folded the observed light curves with the derived period, selecting the zero phase corresponding to the point at which the light curve attains its maximum brightness in the *V* band. First, we derived a function from each template light curve using Fourier series, which will be fitted to the observed light curves. In the case of well-sampled *V*- and *B*-band light curves, we solve for the mean magnitude, amplitude, and a phase offset simultaneously. For the *URI*-band light curves with relatively smaller number of data points, we used amplitude ratios with respect to the *V* band to scale the amplitudes in these filters (Braga et al. 2016). These scaled amplitudes were allowed to vary by ± 10 per cent to account for the uncertainties in the amplitude ratios. Most extreme outliers were removed iteratively during the template-fitting process. The best-fitting templates in *UBVRI* bands were used to determine intensity-averaged mean magnitudes and amplitudes for RR Lyrae variables.

3.3.1 Light curve quality flags

We evaluated the quality of our fitted templates by assigning quality flags based on the mean-squared error (MSE) between the best fit template and observed phased light curves. The MSE is calculated as follows:

$$\text{MSE} = \frac{\sum (m - m_{\text{fit}})^2}{N(m)}, \quad (1)$$

where m is the light curve magnitudes, m_{fit} is the template magnitudes, and $N(m)$ is the number of measurements of magnitudes in the light curve.

Based on a visual inspection of the template fits and MSE values, we defined three quality flags (QF):

- (i) **A**: Phased light curves in a given filter exhibit excellent template fits when MSE is within the range of $0 < \text{MSE} \leq 0.02$.
- (ii) **B**: Phased light curves display some scatter, but they still exhibit clear periodicity and reasonably good template fit when MSE falls in the range of $0.02 < \text{MSE} \leq 0.04$.
- (iii) **C**: Phased light curves exhibit significant scatter, resulting in poor template fits when MSE is greater than or equal to 0.04.

Table 3 shows the derived intensity averaged mean magnitudes and amplitudes in the given filter bands. The Oosterhoff

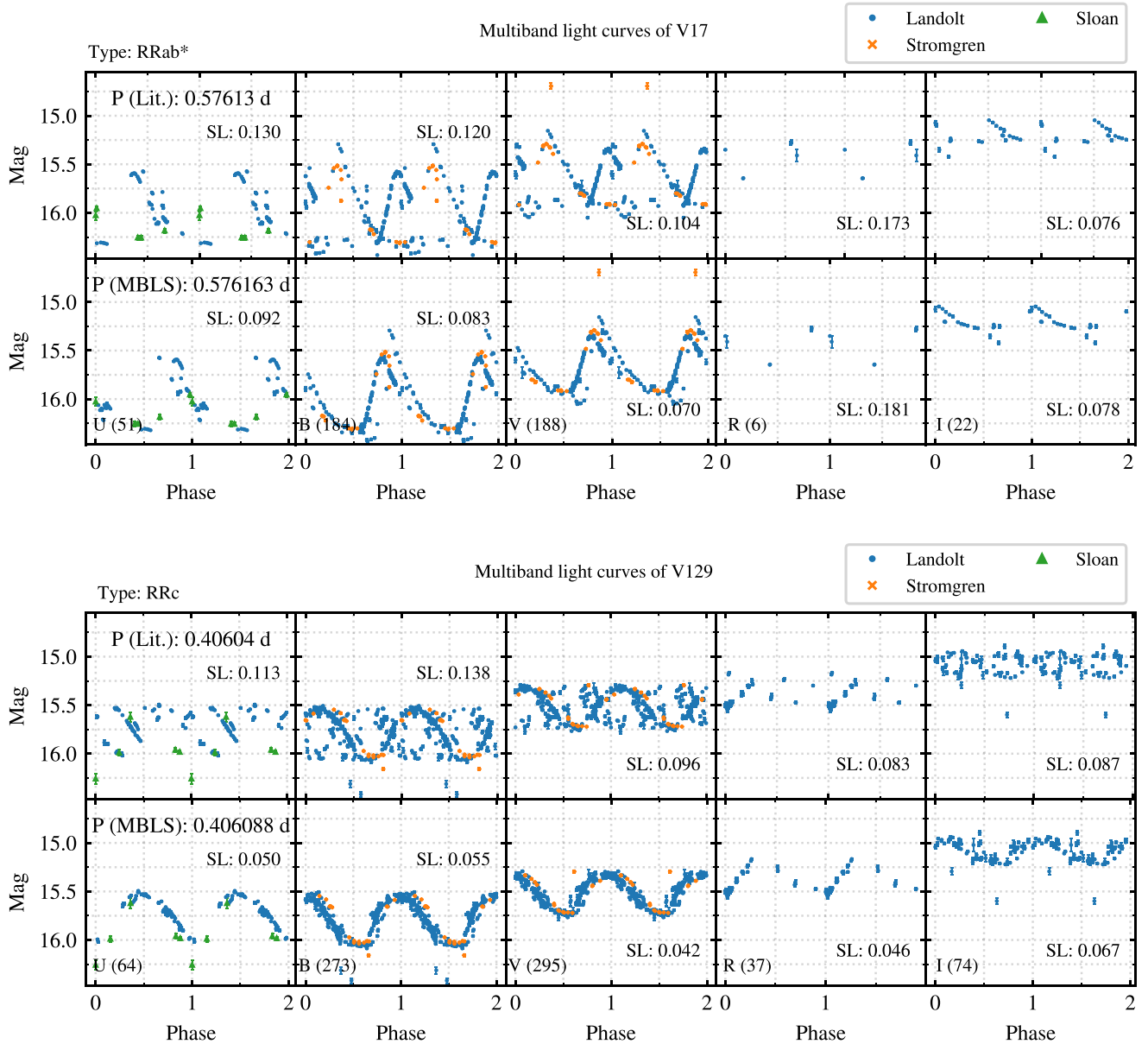


Figure 1. Example phase-folded light curves of V17 and V129 in M3. The upper light curve in each plot is phase-folded using the period derived by Jurcsik et al. (2015, 2017) and Jurcsik (2019). In contrast, the lower light curve in each light curve is phased according to the period obtained through the MBL algorithm. The period difference between the two methods is 0.000033 d for V17 and 0.000048 for V129, and this discrepancy is reflected in the observed differences in the light curves. Within the plot, SL represents the normalized *string length*, indicating the derived period’s accuracy.

classification, Blazhko variability, and subtype for each variable were obtained from Jurcsik et al. 2015, 2017, Jurcsik 2019, and Clement et al. 2001. For cases where we could not find a good template fit, we estimated the mean magnitudes directly from the light curves. The minimum and maximum number of data points utilized to derive the mean magnitudes and amplitudes in *UBVRI* bands are 17, 72, 75, 4, 12 and 64, 277, 295, 40, 95, respectively.

Fig. 4 shows the light curves of two RRAb stars, one being the Blazhko star. The figure also displays the best-fit template. A similar example of light curves and template fits for RRC stars is shown in Fig. 5. A few additional light curves and their corresponding template fits are shown in Figs B1 and B2.

3.4 Colour-magnitude diagrams of M3 with RR Lyrae stars and outlier detection

With the intensity averaged mean magnitudes derived using template fitting, we created CMDs for the M3 stars and the RR Lyrae variables. We have also included infra-red bands (*J*, *H*, and *K_s*) mean magnitudes and amplitudes of M3 RR Lyrae stars from Bhardwaj et al. (2020) for completeness and extending the wavelength range. All the magnitudes were corrected for Galactic extinction $E(B - V) = 0.013$ (VandenBerg, Denissenkov & Catelan 2016) with the conversion factors adopted from Schlegel, Finkbeiner & Davis (1998). All magnitudes in the subsequent analysis are corrected for reddening. The CMD includes only well-measured stars according to the following photometric quality criteria: sources with $\chi < 1.8$,

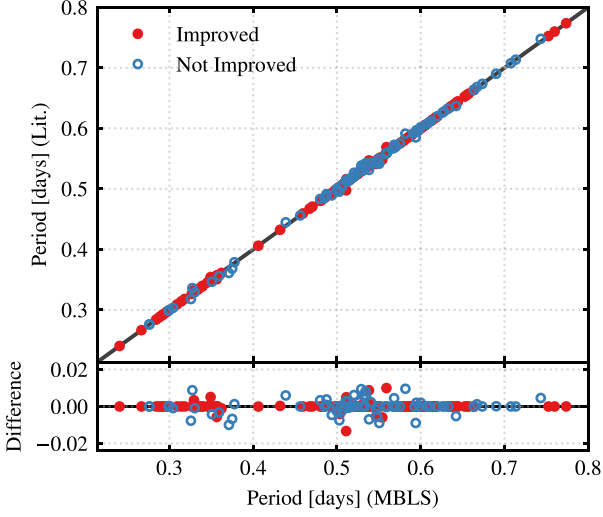


Figure 2. The comparison of periods derived using MBLs and those reported in literature by Jurcsik et al. (2015, 2017) and Jurcsik (2019). The periods were considered improved for stars for which the normalized string length is lower using MBLs periods than with the literature periods.

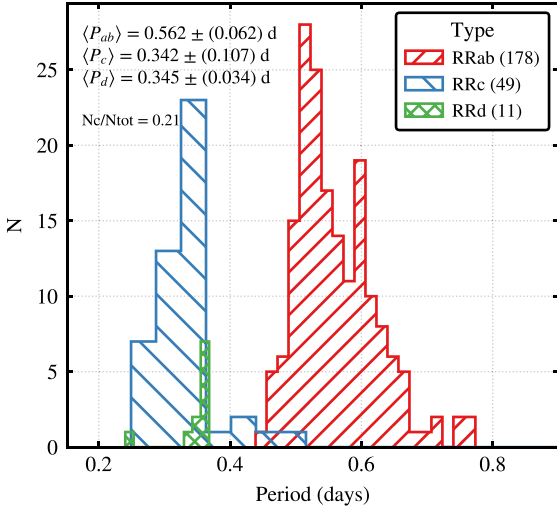


Figure 3. The period distribution of RR Lyrae stars in the M3 globular cluster.

which quantifies the quality of the fit between the observed star’s profile and the PSF characterizing the given image, absolute value of the sharpness parameter (<0.7), which selects stars and rejects objects with too sharp (e.g. cosmic ray or spurious detections around saturated sources) or too broad (e.g. blends or extended sources) PSF, as well as sources with magnitude and colour errors $\sigma_V < 0.03$ mag and $\sigma_{B-I} < 0.04$.

We have also plotted the theoretical blue (hot) edge for first overtone mode pulsators (FOBE) and the red (cool) edge for fundamental mode pulsators (FRE). These edges were determined using the analytical relations proposed by Marconi et al. (2015), assuming a metallicity of $[\text{Fe}/\text{H}] = -1.50$ (corresponding to $Z = 0.00077$) with $[\alpha/\text{Fe}] = 0.20$ and $Y = 0.24$ (Harris 2010). The theoretical instability strip boundaries match the empirical CMD well, but both edges appear redder than the observed distribution of RR Lyrae stars. This

Table 3. Properties of RR Lyrae variables in M3, including their identification (Id), period, intensity averaged mean magnitudes, and amplitudes in the *U*, *B*, *V*, *R*, and *I* filters. The Oosterhoff classification, Blazhko variability, and the quality flags (QF) are also provided. The QF values are given in a sequence for the *UBVR* filter bands, respectively. The complete table can be accessed online in a machine-readable format.

Id	RA ^c	Dec ^c	Type	Blazhko ^b	Period (d)	Oo Type ^b	<U> mag	A _U mag	 mag	A _B mag	<V> mag	A _V mag	<R> mag	A _R mag	<I> mag	A _I mag	QF (UBVR)
V1	13:42:11.12	+28:20:33.8	RRab	–	0.520590 ^b	OoI	15.78	1.31	15.90	1.38	15.62	1.18	15.41	0.81	15.17	0.68	AAAAA
V3	13:42:15.71	+28:21:41.8	RRab	B1	0.558197 ^a	OoII	15.70	1.59	15.85	1.44	15.53	1.25	15.34	0.86	15.09	0.77	AAAAA
V5	13:42:31.29	+28:22:20.7	RRab	B1	0.505834 ^a	OoI	15.97	0.94	15.90	1.42	15.58	1.26	15.55	0.56	15.16	0.83	AAAAA
V6	13:42:02.08	+28:23:41.6	RRab	–	0.514336 ^a	OoI	15.97	1.29	16.00	1.36	15.68	1.14	15.52	0.90	15.24	0.73	AAAAA
V7	13:42:11.09	+28:24:10.2	RRab	B1	0.497423 ^a	OoI	15.97	1.43	15.88	1.47	15.55	1.25	15.52	0.92	15.20	0.74	ABBAA
...
V270n	13:42:11.95	+28:23:32.7	RRab	B1	0.625850 ^b	–	15.77	0.64	15.73	0.95	15.43	0.87	15.28	0.42	14.92	0.44	ABBAA
V271	13:42:12.18	+28:23:17.6	RRab	–	0.632800 ^c	–	16.05	0.88	16.06	0.86	15.66	0.64	15.44	0.15	15.06	0.38	AAAAA
V290	13:42:21.30	+28:23:45.0	RRd	–	0.240413 ^a	–	15.91 [†]	0.25 [†]	15.85 [†]	0.54 [†]	15.67 [†]	0.07 [†]	15.53 [†]	0.22 [†]	15.38 [†]	0.30 [†]	–
V292	13:42:11.18	+28:21:54.0	RRc	–	0.296543 ^a	–	15.81	0.36	15.77	0.37	15.61	0.29	15.45	0.21	15.32	0.21	AAAAA
V299	13:41:18.85	+28:01:57.0	RRc	–	0.249200 ^c	–	15.93 [†]	–	15.80 [†]	–	15.60 [†]	–	–	–	15.42 [†]	–	–

^aThe adopted period was determined using the MBLs algorithm.

^bThe adopted period was sourced from Jurcsik et al. (2017) and Jurcsik (2019) for RRab stars and from Jurcsik et al. (2015) for RRc/RRd stars.

^cThe adopted period as well as RA and Dec values were obtained from Clement et al. (2001).

^dThe adopted period data was extracted from Bhardwaj et al. (2020).

[†]The intensity-averaged mean magnitudes and amplitudes derived directly from the corresponding light curves.

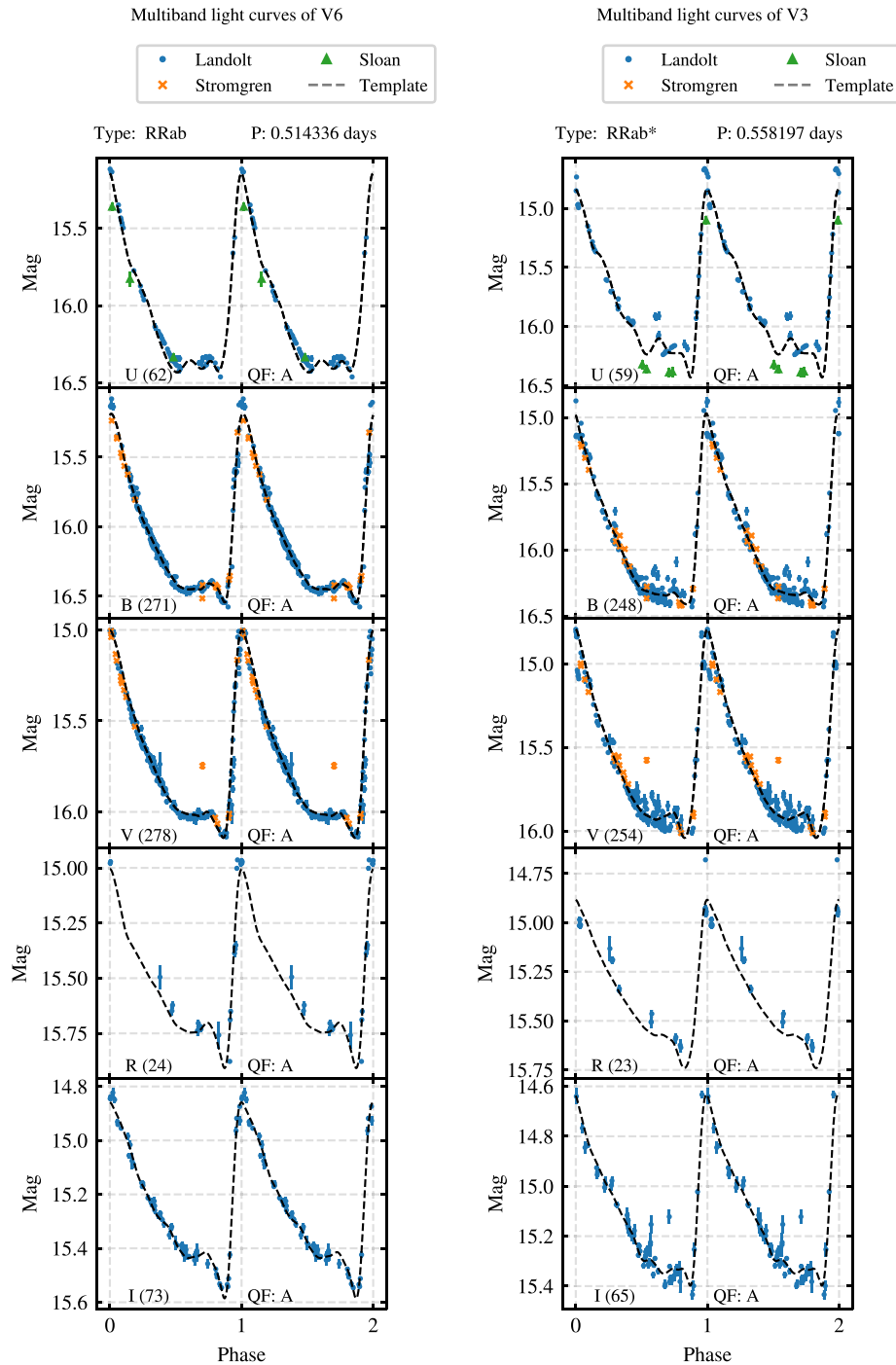


Figure 4. The left-hand panel presents the *U*, *B*, *V*, *R*, and *I* band light curves of V6 (non-Blazhko RRab). The period of this star is determined to be 0.514336 d. The folded light curves of the Blazhko RRab star V3 are displayed in the right-hand panel, with a primary period of 0.558197 d. The best-fitted template is represented by the black curve in both plots. The quantity inside the braces adjacent to the filter name in bottom left corner of each plot represents the total number of observations for the corresponding filter band. The corresponding quality flag (QF) is also given at bottom right corner of each light curve.

slight discrepancy between observed and predicted boundaries can be due to limitations in the current predicted pulsation modelling or the adopted model atmospheres when converting effective temperatures into colours. A better agreement is indeed obtained when the period is adopted in place of the colour. Moreover, the location of the instability edges is known to depend on the efficiency of convection (see e.g. Di Criscienzo, Marconi & Caputo 2004).

To identify potential outliers in these CMDs, we created two ellipses (one for RRab and the other for RRc) in each CMD. The ellipses have the centres at the median of the colour on one axis and the median of the magnitude on the other axis. The eigenvalues and eigenvectors of the covariance matrix of the colour versus magnitude distribution are used to determine the angles of the ellipses. The semimajor and semiminor axis are defined to be 3 times the standard

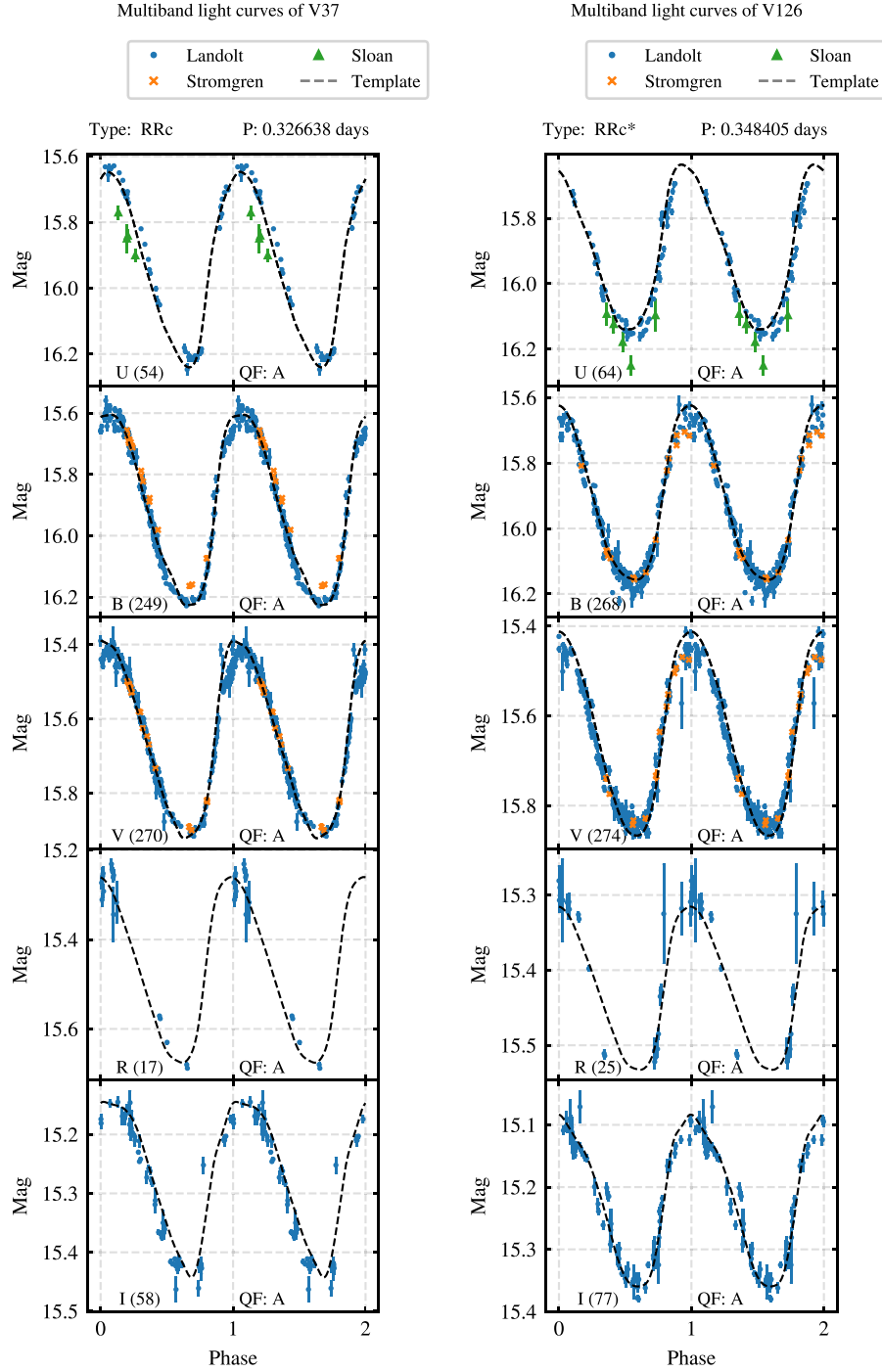


Figure 5. The left-hand panel presents the *U*, *B*, *V*, *R*, and *I* band light curves of the V37 (non-Blazhko RRc) star. The period of this star is 0.326638 d. The folded light curves of the Blazhko RRc star V126 are displayed in the right-hand panel, with a primary period of 0.348405 d. The adopted nomenclature for this figure is same as Fig. 4.

deviation of the distribution in the respective axis. This ellipse creates an artificial boundary for the distribution of the RRab and RRc stars in the CMDs and any star outside this ellipse is marked as a potential outlier (see Fig. 6). We created all possible combinations of CMDs using all available bands: *U*, *B*, *V*, *R*, *I*, *J*, *H*, and *K*, and then marked potential outliers in each of such plots. We did the statistical analysis of the potential outliers from all CMDs and labelled those stars as true

outliers which were outliers in more than 75 per cent of the CMDs. 3 RRc stars (V259, V297, V298) and 9 RRab stars (V113, V115, V123, V159, V193, V194, V205, V249, V270s) were identified as outlier stars and were removed in the subsequent analysis. Their spurious photometric mean magnitudes and amplitudes are also not provided in Table 3. In addition to these, we have excluded stars V4n and V192 from our analysis due to their notably bright *V*-band magnitudes, as

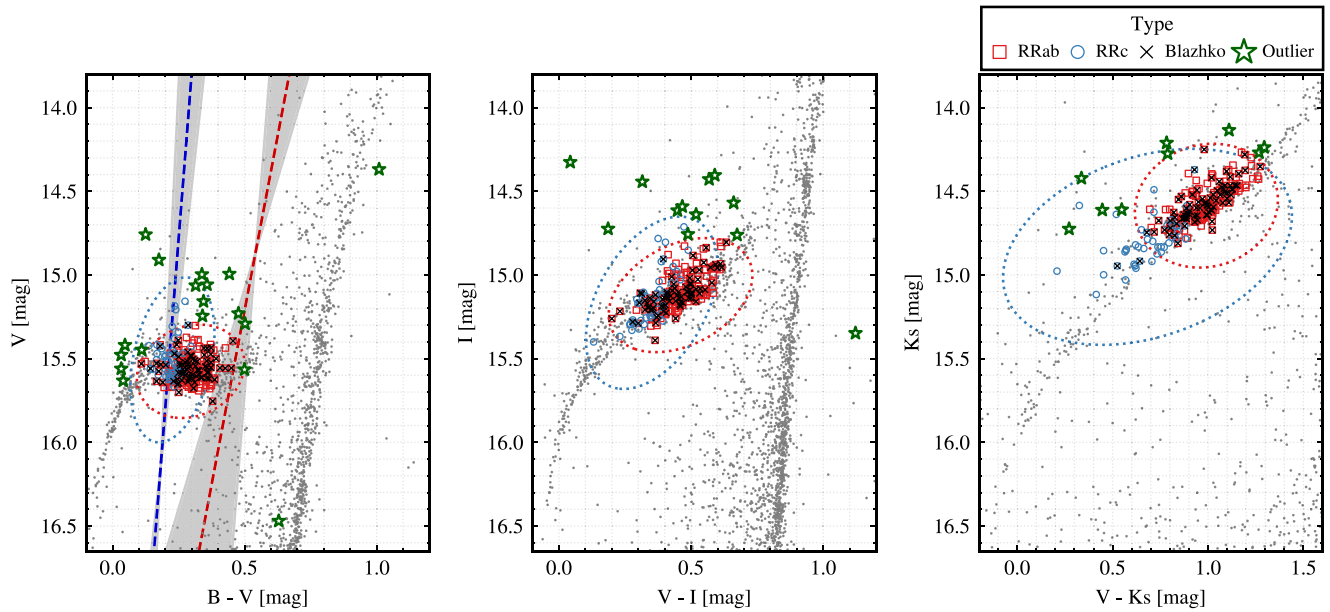


Figure 6. The figure displays the CMDs of M3. The grey points represent all the observed stars in the acquired data set. RRc stars are indicated by blue markers, while RRab stars are represented by red markers. The red and blue dotted lines in the first figure correspond to the theoretical FOBE (first overtone blue edge) and FRE (fundamental mode red edge) obtained using relations from Marconi et al. (2015). The points marked with green star marker are detected outliers in respective CMDs.

directly calculated from their light curves. These magnitudes are inconsistent with the expected magnitudes of horizontal branch stars within the M3 cluster.

3.5 Bailey diagrams and the amplitude ratios

The specific pulsation mode of RR Lyrae stars can be determined by their position on a luminosity amplitude-logarithmic period plane, commonly referred to as Bailey’s diagram (Bailey 1902). Bailey’s diagram for the M3 cluster is shown in Fig. 7 for all wavelength bands. We have plotted a solid line for OoI and a dotted line for OoII RRab stars to represent the locus of Oosterhoff-type stars. These were generated using the following equation provided by Cacciari et al. (2005). For RRab OoI-type stars,

$$A_B = -3.123 - 26.331(\log P) - 35.853(\log P)^2, \quad (2)$$

and for RRab OoII, the same equation holds with $\Delta \log P = 0.06$. For RRc, we used the relation,

$$A_V = -9.75 + 57.3 \times P - 80.0 \times P^2, \quad (3)$$

given by Kunder et al. (2013). Additionally, the correlation between the amplitudes of RR Lyrae stars at different wavelengths is evident with a decrease in amplitudes at longer wavelengths. The graph illustrates the well-known property of pulsating stars’ amplitudes decreasing as the wavelength increases (see also Bhardwaj et al. 2017; Das et al. 2018).

In line with the methodology employed by Kunder et al. (2013), Stetson et al. (2014a), and Braga et al. (2016), we also calculated the amplitude ratios in different bands. Fig. 8 illustrates the obtained amplitude ratios relative to the V band for RRab and RRc stars in M3. We found that the amplitude ratios exhibited similar values (within the error bars) for both types of stars. Moreover, we observed no difference in the amplitude ratio between short-period ($P_{ab} \leq 0.6$ d)

and long-period ($P_{ab} \geq 0.6$ d) RRab stars in contrast with findings from NIR light curves (Bhardwaj et al. 2020). The overall amplitude ratio values are in line with literature values from Braga et al. (2016) for ω Cen and other GCs (Di Criscienzo et al. 2011; Kunder et al. 2013; Stetson et al. 2014a). Table 4 provides the estimated amplitude ratios in different bands.

While Inno et al. (2015) proposed a possible dependence of amplitude ratios on metallicity for Cepheids, recent studies conducted on several clusters with diverse metallicities have revealed no clear correlation of amplitude ratios with metallicity (Braga et al. 2016) for RR Lyrae stars. Notably, despite their different metallicities, the amplitude ratios for M3 and ω Cen (derived by Braga et al. 2016) are found to be consistent, further supporting the absence of dependence on metallicity.

4 M3 RR LYRAE: PERIOD–LUMINOSITY, WESENHEIT RELATIONS, AND A DISTANCE DETERMINATION

4.1 Period–luminosity (PL) relations

RR Lyrae exhibit a well-defined PLR in near-infrared wavelength bands (Longmore et al. 1986; Bhardwaj et al. 2020, and references therein) but do not obey any defined relation in optical wavelength bands (UBV) either in empirical data (Benkő, Szabó & Paparó 2011; Braga et al. 2015) or in theoretical models (Bono et al. 2001; Catelan 2004a; Marconi et al. 2015).

We utilized the periods and extinction corrected intensity averaged mean magnitudes obtained in Section 3.3 to derive PLRs for the R and I bands. The PLRs are fitted to the data, assuming the mean magnitudes vary linearly with the log period. The following equation is fitted to the data,

$$m_\lambda = b_\lambda \log(P) + a_\lambda, \quad (4)$$

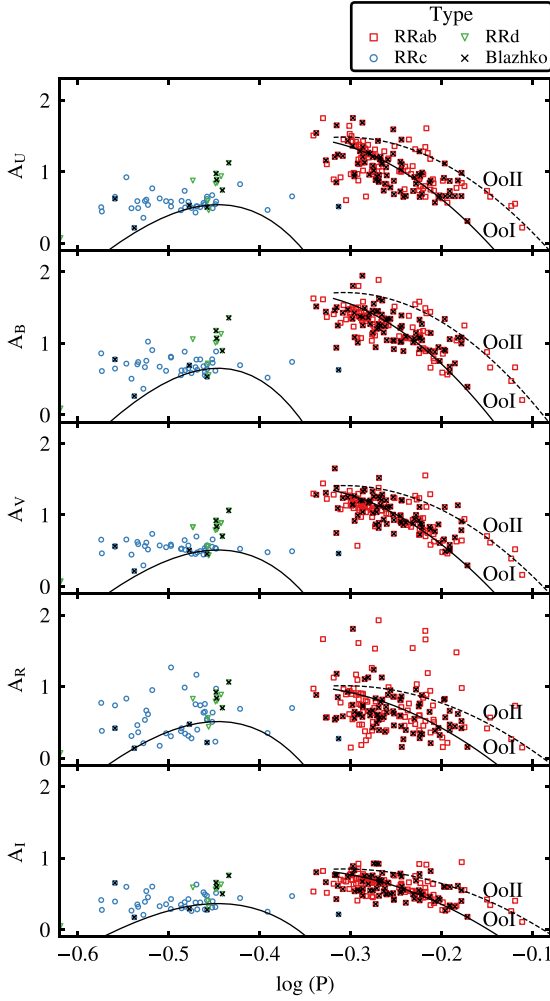


Figure 7. The figure illustrates Bailey’s diagram, depicting the period versus amplitude relationship for different filter bands in M3. In addition, the lines are included in the plot for each star type, representing the Oosterhoff-type locus. The equations used to generate these lines are based on Cacciari et al. (2005) for RRab OoI and RRab OoII locus was derived using the same equation but with a $\Delta \log P$ of 0.06. The relation provided by Kunder et al. (2013) is utilized for RRC stars.

Here, a_λ and b_λ are the zero-point and slope of the PLR in a given filter λ . The scatter (rms) in the PLRs is a consequence of the intrinsic width of the instability strip in temperature (Marconi et al. 2015). It may also arise due to the metallicity spread of the RR Lyrae in clusters and the uncertainties in extinction correction. However, M3 stars do not show a significant metallicity spread ($\sigma_{[\text{Fe}/\text{H}]} \sim 0.03$ dex, Sneden et al. 2004). Fig. 9 represents the distribution of mean magnitudes with the logarithmic period in the I and R bands. In the left-hand panel of plot, we show the $\log(P)$ versus mean magnitude in the respective band for RRab and RRC stars, and in the right-hand panel, the global PL relation is shown for I and R bands. An iterative linear fit is performed by removing the outlier stars ($\geq 3\sigma$) to get the slope and intercept of the PLR for both RRab and RRC stars. Global PLRs were also derived by fundamentalizing the periods of RRC variables using the relation (Iben & Huchra 1971; Rood 1973; Cox, Hodson & Clancy 1983; Di Criscienzo et al. 2004; Coppola et al. 2015),

$$\log P_{\text{FU}} = \log P_{\text{FO}} + 0.127, \quad (5)$$

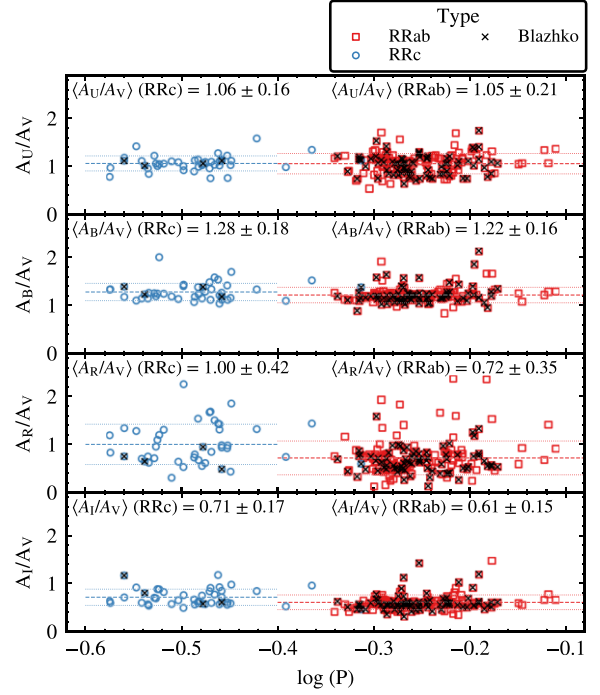


Figure 8. The figure illustrates the distribution of the luminosity amplitude ratio, relative to the V -band luminosity amplitude, as a function of the period of the stars.

Table 4. Mean amplitude parameter ratio (with respect to V -band amplitude) and associated standard deviation for the RRL stars in the M3 globular cluster.

	RRab		RRC	
	mean	std	mean	std
$\frac{A_I}{A_V}$	1.05	0.21	1.06	0.16
$\frac{A_B}{A_V}$	1.22	0.16	1.28	0.18
$\frac{A_R}{A_V}$	0.72	0.35	1.00	0.42
$\frac{A_U}{A_V}$	0.61	0.15	0.71	0.17

where ‘FU’ refers to the fundamental mode and ‘FO’ represents the first-overtone mode.

Table 5 lists the values of slopes and zero-points of the PLRs for RRC and RRab stars as well as global relations. These empirical relations are best constrained in the I band with a scatter of only 0.149 mag for RRC stars, 0.107 mag for RRab, and 0.124 mag for the combined sample of RRab and RRC stars.

4.2 Period–Wesenheit (PW) relations

The Wesenheit index is defined as a combination of multiple passband magnitudes of a star in a way that effectively eliminates the impact of reddening. The Wesenheit index was initially developed to study Cepheid variable stars’ PLRs (Madore 1982). Over time, the application of the Wesenheit index has expanded beyond Cepheids and has been used in various studies of different types of variable stars, including RR Lyrae stars, which are crucial for distance determinations in globular clusters and studies of stellar populations in galaxies (Neeley et al. 2019; Mullen et al. 2023).

We adopted the same Wesenheit magnitudes constructed for theoretical models in Marconi et al. (2015). We derive empirical PW relations in the form of equation (4) following the same process

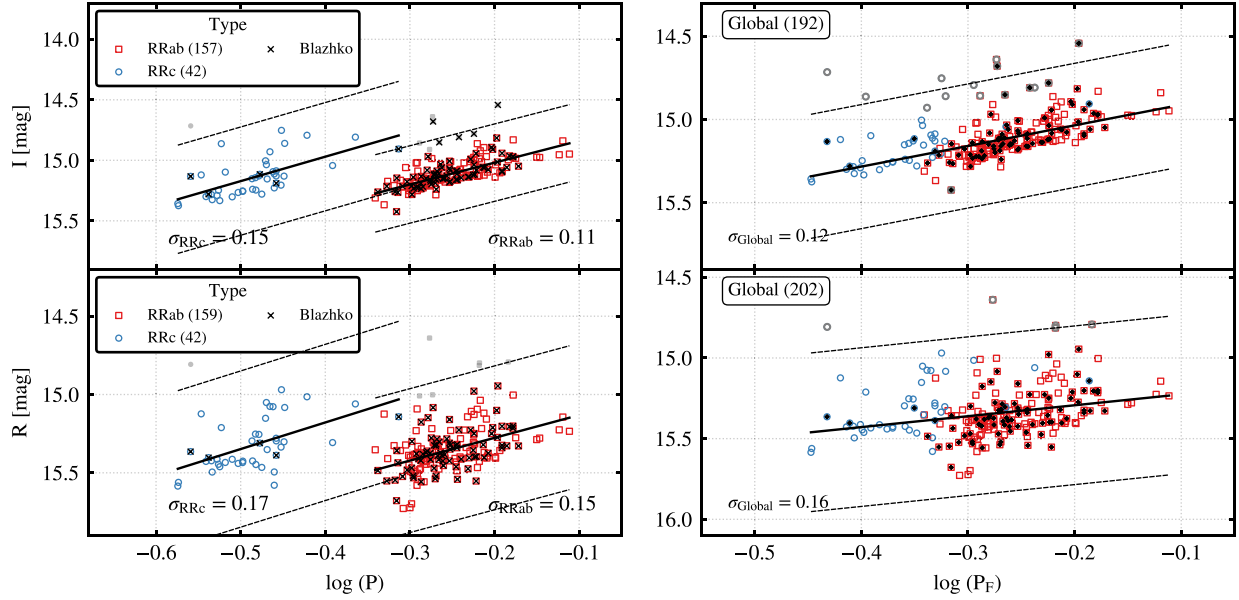


Figure 9. This figure shows the PLRs for the I and R bands. In the right-hand panel, P_F represents the period resulting from the conversion of ‘FO’ mode periods into ‘FU’ mode using equation (5). The scatter in the PLRs is represented by σ . The solid line represents the fitted PLR, and the region of $\pm 3\sigma$ is represented by the dashed lines.

Table 5. PLR for I and R band: $m_\lambda = b_\lambda \log(P) + a_\lambda$.

λ	N	RRab			σ	N	RRc			σ	N	Global		
		b_λ	a_λ	σ			b_λ	a_λ	σ			b_λ	a_λ	σ
I	157	-1.804 ± 0.004	14.659 ± 0.001	0.107	42	-2.020 ± 0.007	14.162 ± 0.003	0.149	192	-1.239 ± 0.003	14.788 ± 0.001	0.124		
R	159	-1.453 ± 0.005	14.986 ± 0.001	0.153	42	-1.698 ± 0.009	14.499 ± 0.004	0.166	202	-0.677 ± 0.003	15.158 ± 0.001	0.164		

described above for the PL relations. We incorporated the mean magnitudes of M3 RR Lyrae stars in NIR bands (J , H , and K_s) from Bhardwaj et al. (2020) to establish optical, optical-NIR double, and triple band PW relations. Fig. 10 shows dual band Wesenheit indices plotted against the log period. The plot shows the period versus Wesenheit indices separately for RRab and RRc stars, and the global sample of all RR Lyrae variables. Table 6 contains the coefficients, their corresponding errors, and the standard deviations of the optical and optical-NIR dual and triple band PW relations for RR Lyrae stars in the M3 cluster.

4.3 Distance to M3

Using the derived PW relations for FU, FO, and the global sample of stars, we calculated the distances to each RR Lyrae star and then determined the mean distance to the M3 cluster. To do this, we employed the metal-independent PW(V , $B - V$) relation provided by Marconi et al. (2015) as an absolute calibration and compared it with the observed PW(V , $B - V$) relation. As the M3 globular cluster is a mono-metallic cluster with $[\text{Fe}/\text{H}] \sim -1.5$ dex (Harris 2010) and a small metallicity spread of $\Delta[\text{Fe}/\text{H}] \sim 0.03$ dex (Snedden et al. 2004), the effect of metallicity on distances derived using the PW relation is negligible. However it should be noted that the recent analysis by Lee & Sneden (2021) revealed a bimodal distributions in two populations, with $\langle[\text{Fe}/\text{H}]\rangle \approx -1.60$ and -1.45 dex. Since PW relations are independent of reddening, they are known for their accuracy in deriving distances of RR Lyrae stars (Braga et al. 2015, 2016; Bellinger et al. 2020; Kumar et al. 2023).

Through a comparison of the metal-independent theoretical calibrations by Marconi et al. (2015) with the observed slopes and zero-points, we obtained distance moduli (μ) to M3 of 15.03 ± 0.03 (statistical) ± 0.12 (systematic) mag for FU, $15.05 \pm 0.04 \pm 0.30$ mag for FO, and $15.05 \pm 0.04 \pm 0.08$ mag for the global sample. The statistical error accounts for the dispersion in the distribution of individual RR Lyrae star distance moduli. In contrast, the systematic error reflects the discrepancy between the theoretical and semi-empirical calibration of the PW(V , $B - V$) relations. Final estimates of the distance moduli are derived by taking average of μ_{RRab} , μ_{RRc} , and μ_{Global} . The resulting distance modulus using metal-independent theoretical calibrations is $\mu = 15.04 \pm 0.19(\text{sys.}) \pm 0.04(\text{stats})$ mag. The estimates agree within 1σ of the combined statistical and systematic errors for all samples of RR Lyrae stars.

Using the metal-dependent PW(I , $V - I$) relation and adopting $[\text{Fe}/\text{H}] = -1.53$ dex, we derived the distance to M3. Employing the theoretical relations from Marconi et al. (2015), we obtained the following distance moduli: $15.05 \pm 0.06 \pm 0.08$ mag for FU stars, $15.01 \pm 0.02 \pm 0.28$ mag for FO stars, and $15.05 \pm 0.03 \pm 0.06$ mag for the global sample. The estimated distance modulus using metal-dependent theoretical calibrations is $\mu = 15.03 \pm 0.17(\text{sys.}) \pm 0.04$ mag. Notably, both the metal-dependent and metal-independent estimates show agreement within the respective given standard errors. This outcome was expected, as the M3 cluster is characterized by being mono-metallic, with a minimal spread in its metallicity distribution. In a study of NIR photometry of RR Lyrae stars in M3, Bhardwaj et al. (2020) derived the distance to the M3 cluster using the theoretically predicted absolute calibrations of PL-metallicity relations in JHK_s bands, yielding a distance modulus of

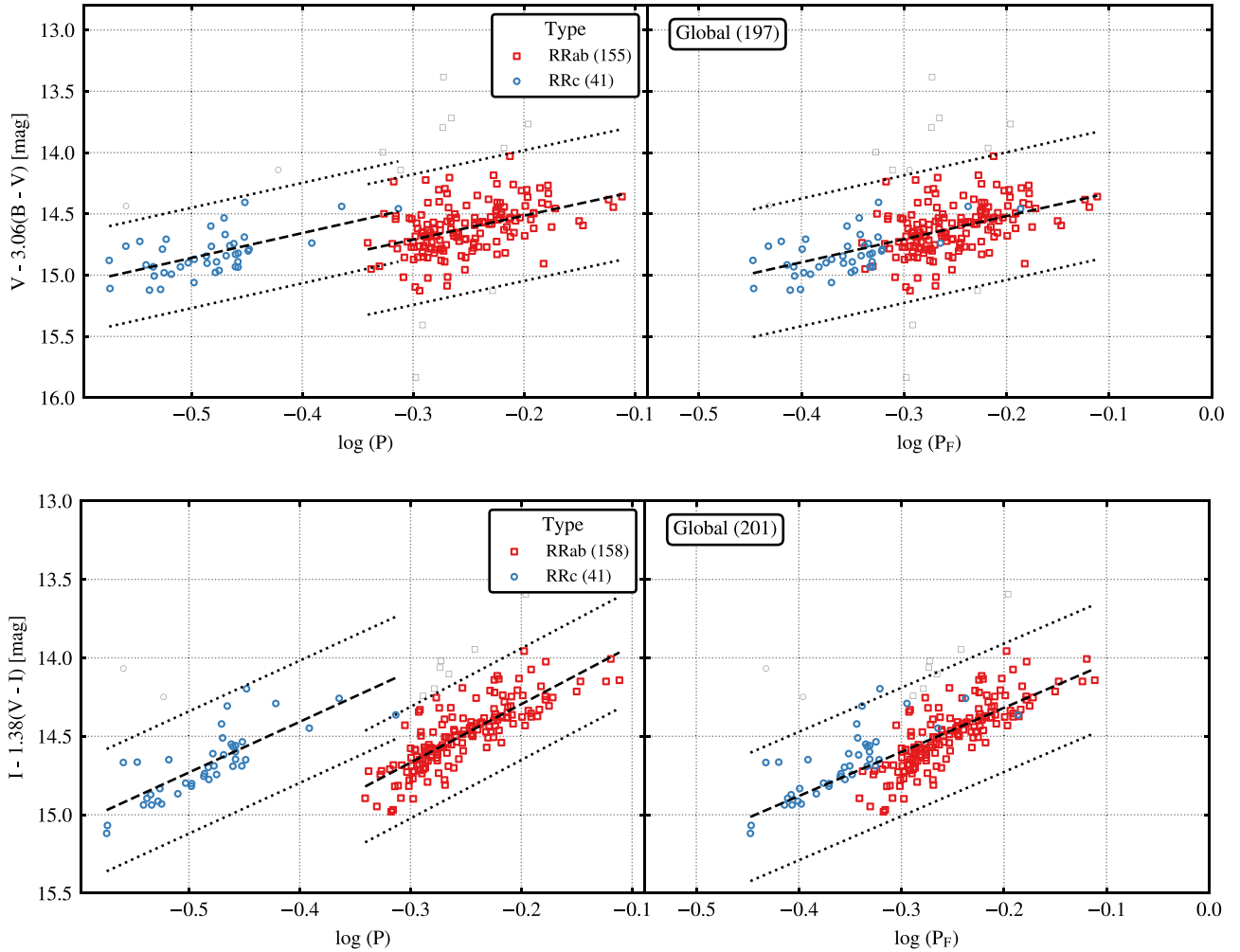


Figure 10. Empirical dual band PW relations for M3 RR Lyrae stars. The fitted PW relation is represented by the dashed line, and the region of $\pm 3\sigma$ is represented by the dotted lines.

$\mu = 15.041 \pm 0.017$ (stat.) ± 0.036 (syst.) mag. Our results based on optical photometry are also in excellent agreement with those based on near-infrared photometry (e.g. Bhardwaj et al. 2023).

5 STELLAR PARAMETERS FOR RR LYRAE STARS IN M3

5.1 Fourier analysis of RR Lyrae stars in M3

The shape of RR Lyrae stars' light curves contains useful information about their intrinsic properties. Previous studies, such as those by Simon & Clement (1993), Kovacs & Zsoldos (1995), Jurcsik & Kovács (1996), Kovács & Jurcsik (1996), Kovacs & Kanbur (1998), Deb & Singh (2009), Bhardwaj et al. (2015), and Das et al. (2018) have investigated the correlation between Fourier parameters, as well as period, with intrinsic properties like mass, luminosity, metallicity, and colours.

In our study, we have an extensive collection of photometric data for M3, covering all optical bands. Leveraging this data set, we derived the Fourier parameters for individual RR Lyrae light curves by fitting a Fourier series of sines to each light curve. Specifically, we applied a Fourier sine series to the light curves in filter bands

with substantial phase coverage, namely the *B*, *V*, and *I* bands. The Fourier parameters were derived using the following equation:

$$m = m_0 + \sum_{k=1}^N A_k \sin(2k\pi \cdot x + \phi_k), \quad (6)$$

For a specific filter band, m represents the magnitude of the star at a given phase x , m_0 represents the mean magnitude, and A_k and ϕ_k represent the Fourier amplitude and phase coefficients, respectively. Here, N is the order of fit, and we chose $N = 5$, to fit the light curves.

We calculated the Fourier amplitude ratios (R_{k1}) and phase differences (ϕ_{k1}) using the following equations:

$$R_{k1} = \frac{A_k}{A_1}, \quad \phi_{k1} = \phi_k - k\phi_1, \quad (7)$$

Here, k is an integer greater than 1, and $0 \leq \phi_{k1} \leq 2\pi$. The errors associated with the Fourier parameters were calculated using error propagation methods applied to the Fourier coefficients. The Fourier amplitude ratios and phase differences for RR Lyrae in M3 along with the scatter (σ), are given in Table 7 for the *BVI* bands.

Fig. 11 illustrates the relationship between the Fourier parameters (R_{21} , R_{31} , ϕ_{21} , ϕ_{31} ...) and the period of RR Lyrae stars in M3

Table 7. The table presents the Fourier coefficients, along with their corresponding standard deviations, for the RR Lyrae stars in the M3 globular cluster, categorized according to the specified filter band. The complete table can be accessed online in a machine-readable format.

Id	Type	Period	Band	N	R_{21}	Φ_{21}	R_{31}	Φ_{31}	R_{41}	Φ_{41}	R_{51}	Φ_{51}	σ
V1	RRab	0.520590	B	271	0.415 ± 0.012	1.996 ± 0.032	0.316 ± 0.012	4.561 ± 0.046	0.204 ± 0.011	0.831 ± 0.065	0.183 ± 0.012	3.294 ± 0.075	0.085
V1	RRab	0.520590	V	276	0.456 ± 0.010	2.101 ± 0.023	0.361 ± 0.009	4.660 ± 0.033	0.245 ± 0.008	0.824 ± 0.047	0.200 ± 0.009	3.454 ± 0.056	0.066
V1	RRab	0.520590	I	75	0.476 ± 0.026	2.521 ± 0.061	0.395 ± 0.019	5.197 ± 0.092	0.229 ± 0.018	1.760 ± 0.139	0.142 ± 0.018	4.462 ± 0.175	0.055
V3	RRab	0.558197	B	250	0.440 ± 0.010	2.299 ± 0.032	0.324 ± 0.011	4.892 ± 0.045	0.223 ± 0.011	1.345 ± 0.056	0.170 ± 0.010	4.165 ± 0.077	0.076
...
V271	RRab	0.632800	I	35	0.464 ± 0.026	3.051 ± 0.079	0.224 ± 0.024	5.908 ± 0.151	0.138 ± 0.028	2.899 ± 0.202	0.086 ± 0.027	6.018 ± 0.319	0.035
V292	RRc	0.296543	B	262	0.071 ± 0.017	2.933 ± 0.242	0.022 ± 0.017	0.488 ± 0.796	0.020 ± 0.017	6.119 ± 0.868	0.045 ± 0.016	0.200 ± 0.397	0.035
V292	RRc	0.296543	V	276	0.099 ± 0.022	3.522 ± 0.196	0.057 ± 0.021	2.126 ± 0.369	0.067 ± 0.023	2.175 ± 0.290	0.042 ± 0.021	3.466 ± 0.484	0.042
V292	RRc	0.296543	I	66	0.163 ± 0.038	3.433 ± 0.277	0.178 ± 0.046	1.559 ± 0.240	0.034 ± 0.042	4.046 ± 1.255	0.137 ± 0.041	1.067 ± 0.355	0.031

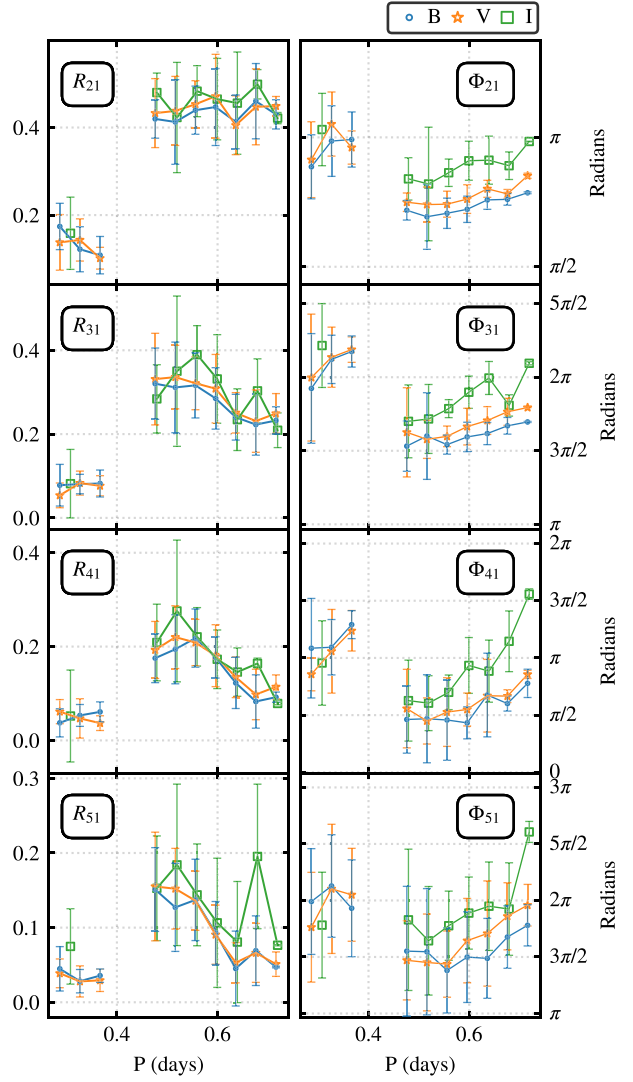


Figure 11. In this plot, the distribution of Fourier parameters is depicted alongside the period for RR Lyrae stars. Each data point represents the mean value of the Fourier parameter within a specific period bin, with error bars indicating the standard deviation in that corresponding period bin. The Fourier amplitude ratio parameters and the Fourier phase difference parameters are binned using a period bin size of 0.04 d.

for each optical band light curve. The plot represents the mean Fourier parameters within each period bin, with the error bars indicating the standard deviation in that bin. The Fourier phase parameter (ϕ_{31}), as discussed by Jurcsik & Kovács (1996), is an important parameter due to its dependence on the pulsation period and metallicity. We observe a linear relation between ϕ_{31} and the period, which is consistent with previous findings by Jurcsik et al. (2017) for V-band light curves. Moreover, Fourier phase parameters increase with wavelength, a trend that is seen for both RR Lyrae (Das et al. 2018) and Cepheid variables (Bhardwaj et al. 2015, 2017).

5.2 Physical parameters of non-Blazhko RRab stars using artificial neural network (ANN)

Physical parameters of RR Lyrae stars are usually derived using the empirical relations between various properties of a light curve

like Fourier parameters, colour, etc., along with the period (Cacciari et al. 2005; Deb & Singh 2010; Nemeč et al. 2011). However, with the advancements in the theoretical modelling of stellar pulsation, it has been possible to generate a grid of models to study the properties of RR Lyrae and other variable stars (Marconi et al. 2015; De Somma et al. 2020, 2022). The radial stellar pulsations (RSP) code of Smolec & Moskalik (2008) as a module in Modules for Experiments in Stellar Astrophysics (MESA, Paxton et al. 2011, 2013, 2015, 2018, 2019) is also available and can be used to generate new theoretical models. Such models are then used to constrain the physical properties of RR Lyrae stars, including their physical parameters like (mass, luminosity, effective temperature, etc).

The physical parameters of RR Lyrae can also be inferred by comparing the light curves of observed stars with a reference library of models. Das et al. (2018) derived the physical parameters of a few RRab stars in the large magellanic cloud (LMC) by comparing the observed light curves with the theoretical model light curves provided by Marconi et al. (2015). A drawback of the method is that only a small number of LMC light curves could be matched with theoretical models.

Another approach to derive the physical parameters using theoretical models is to use a denser and smoother grid of models with non-linear optimization methods (Bellinger et al. 2016). However, the models require a high amount of computational resources for computing even just a single light curve, and it is thus not feasible to generate a smooth and dense grid. To overcome this problem, Kumar et al. (2023) trained an ANN on the physical parameter light curve model grid of Marconi et al. (2015) for RRab stars in V and I bands. The trained neural network² can generate a much smoother and denser grid of theoretical models, and one light curve takes only ~ 55 ms to generate.

Taking into account, the predicted evolutionary properties of RR Lyrae for the adopted metal abundance ($Z = 0.001$, which corresponds to $[\text{Fe}/\text{H}] = -1.54$ dex), we used the ANN interpolator to generate a grid of RRab models with $M = 0.58\text{--}0.64 M_{\odot}$, with a step size of $0.003 M_{\odot}$, $\log(L/L_{\odot}) = 1.67\text{--}1.99$ dex, with a step size of 0.016 dex, and an effective temperature ranging from $5700\text{--}6900$ K with a step size of 60 K. We fixed the hydrogen abundance ratio, X to 0.754 . The selection of limits for the stellar parameters was guided by the boundaries defined within the parameter space of the models of Marconi et al. (2015). This choice aligns with the fact that the ANN is trained exclusively on these models and may struggle to generate accurate light curves for parameters lying beyond the boundaries of the original grid. We generated 8000 new V -band light curves with the given combination of mass, luminosity, and temperature.

To derive the physical parameters of the observed RRab stars in the M3 cluster, we generated a grid of models and compared them to the observed V -band light curves because they have the best sampling. The relationship between the light curve (y) and the corresponding physical parameters (x) is represented by a function (f), such that $y \equiv f(x)$. Conversely, an inverse function (g) exists, enabling the representation of x in terms of y , i.e. $x \equiv f^{-1}(y) \equiv g(y)$. ANNs serve as effective function approximators when the functions are continuous and differentiable (Cybenko 1989; Hornik, Stinchcombe & White 1989; Hornik 1991).

Table 8. The hyperparameter search space for the ANN.

S. N.	Name of hyperparameter	Possible values
1	Number of hidden layers	[1, 2, 3]
2	Number of neurons in one hidden layer	[16, 32, 64, 128]
3	Optimizer	'adam' (Kingma & Ba 2014)
4	Learning rate	$[10^{-2}\text{--}10^{-4}]$ (log sampling)
5	Activation function	['relu', 'tanh']
6	Weights initialization	'GlorotUniform'

In this study, an ANN called *RRab-Net* is trained using 8000 newly generated models to approximate the function 'g'. The selection of architecture and hyperparameters in our study was typically based on expert intuition and manual tuning. We utilized a trial-and-error approach, random grid search (Bergstra & Bengio 2012), to determine these characteristics. A grid of possible hyperparameter combinations is tabulated in Table 8. From these combinations, we randomly selected a set of 200 hyperparameter combinations. The network was then trained for a fixed 1000 epochs using the L2 norm (MSE) as the objective function and the adaptive moment stochastic gradient descent (or adam: Kingma & Ba 2014 algorithm with a default batch size of 32 samples) as an optimization algorithm. The optimization of the network architecture was performed using the KerasTuner³ (O'Malley et al. 2019) module of PYTHON. The final network architecture adopted for the training of *RRab-net* consists of three hidden layers with 128, 64, and 64 neurons, respectively, in those layers, as detailed in Table A1. The details of the final training of *RRab-Net* are discussed in Appendix A.

The accuracy of the predicted physical parameters is assessed by comparing the observed light curves with those generated by the ANN interpolator, a neural network trained by Kumar et al. (2023). If the generated light curve closely matches the observed light curve, it validates the accuracy of the inferred physical parameters. The MSE and correlation coefficient (R^2) are utilized as metrics to assess the similarity between the predicted and observed light curves. Based on the metrics employed, our findings indicate that the ANN can successfully predict light curves that closely resemble the observed light curves for many stars. However, it is essential to note instances where the predicted and observed light curves do not align. This can be attributed to certain limitations in our approach. As our initial network is trained on a finite grid of models, it might not encompass the full range of possible physical parameter combinations. Consequently, when dealing with observed light curves associated with physical parameters falling beyond the scope of our training grid, our method might yield less accurate estimations of these parameters.

Fig. 12 illustrates the ANN-predicted light curve in the V band, along with the inferred physical parameters for variable V109. The period, along with other physical parameters, is employed as input to generate the light curve. The observed light curve is scaled to absolute magnitude using the distance modulus derived in Section 4.3. Note that the higher amplitude of theoretical light curves is a systematic in stellar pulsation models that can be mitigated by assuming a higher efficiency of convection (Bhardwaj et al. 2017).

The masses (M/M_{\odot}), luminosities (expressed as $\log(L/L_{\odot})$), and effective temperatures (T_{eff}) of non-Blazhko RRab stars have been deduced by analysing their V -band light curves. These parameters

²The trained ANN networks can be accessed online on <https://ann-interpolator.web.app/>.

³https://keras.io/keras_tuner/.

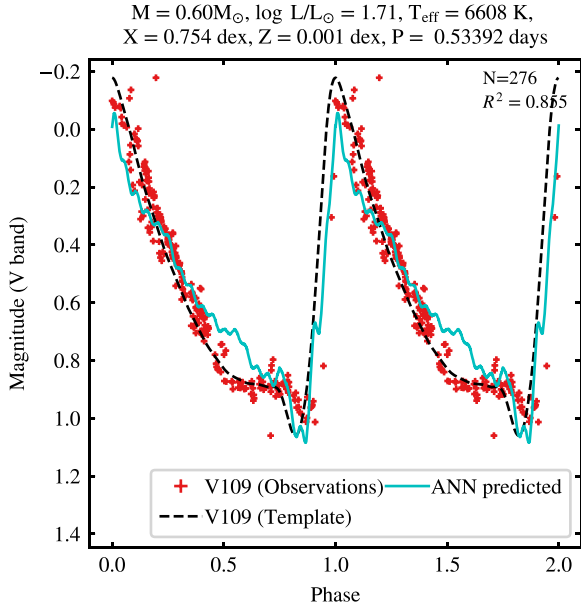


Figure 12. This figure displays the observed and ANN-predicted light curve of V109. The ANN-predicted light curve is generated using the ANN interpolator introduced by Kumar et al. (2023). The input parameters for the ANN interpolator are derived from *RRab-Net*.

Table 9. This table presents the predicted parameters for non-Blazhko RRab variables obtained through the application of *RRab-Net* on their *V*-band light curves. In this table, σ represents the MSE, and R^2 signifies the correlation coefficient between the light curve predicted by the ANN interpolator and the template fitted to the original observations. The complete table can be accessed online in a machine-readable format.

Id	M/M_{\odot}	T_{eff} (K)	$\log(L/L_{\odot})$ (dex)	σ	R^2
V1	0.617	6674	1.696	0.018	0.864
V6	0.612	6658	1.677	0.013	0.894
V9	0.610	6545	1.686	0.010	0.900
V11	0.623	6651	1.702	0.020	0.857
⋮	⋮	⋮	⋮	⋮	⋮
V254	0.594	6432	1.765	0.013	0.721
V257	0.601	6593	1.783	0.008	0.899
V258	0.591	6413	1.717	0.013	0.689
V262	0.602	6465	1.743	0.012	0.673

are provided in Table 9, while their distributions are shown in Fig. 13. The average mass, luminosity, and effective temperature are $M = 0.605 \pm 0.009 M_{\odot}$, $\log(L/L_{\odot}) = 1.71 \pm 0.04$ dex, and $T_{\text{eff}} = 6571 \pm 83$ K. In Fig. 14, the derived effective temperatures are plotted against the colour ($V - I$) of the non-Blazhko RRab stars, and we found the expected correlation between them.

Several literature studies have explored the stellar parameters of non-Blazhko RRab stars in M3. Cacciari et al. (2005) utilized colour-temperature calibrations to derive parameters for V72, yielding values of $M = 0.72 \pm 0.05 M_{\odot}$, $\log(L/L_{\odot}) = 1.67 \pm 0.03$, and $T_{\text{eff}} = 6773 \pm 100$ K. Marconi & Degl’Innocenti (2007) conducted a comprehensive analysis of M3 RR Lyrae stars, including V128, V126, V72, and V152. However, only V72 is a non-Blazhko RRab star among these RR Lyrae variables. They determined the following properties for this star: M ranging from 0.60 to 0.73 M_{\odot} , $\log(L/L_{\odot})$

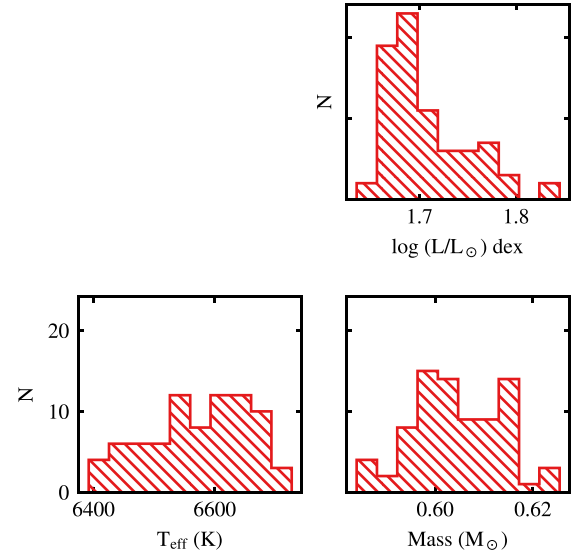


Figure 13. This figure presents histograms depicting the predicted mass, luminosity, and effective temperature derived from the *V*-band light curves with *RRab-Net*.

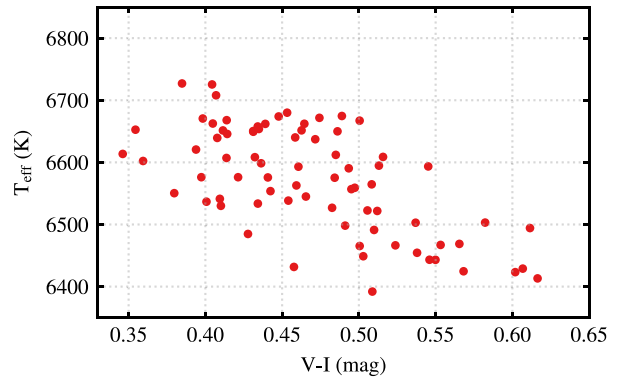


Figure 14. In this figure, the colour ($V - I$) of stars is plotted against the derived effective temperature using *RRab-Net*.

spanning between 1.643 and 1.710 dex, and T_{eff} ranging from 6900 to 7000 K. However, in our study, focusing on the same star, we obtained slightly different values: $M = 0.60 M_{\odot}$, $\log(L/L_{\odot}) = 1.67$, and $T_{\text{eff}} = 6563$ K. In a related study, Valcarce & Catelan (2008) investigated the mass distribution of horizontal branch stars within M3. Employing a semi-empirical approach, they determined a mass distribution for non-Blazhko RRab stars, yielding a value of $0.644 \pm 0.005 M_{\odot}$ for the masses of those stars. In contrast, our analysis using *V*-band light curves predicted a mass distribution of $0.605 \pm 0.009 M_{\odot}$. These discrepancies emphasize the complexities and challenges inherent in determining precise physical parameters, likely arising from varying methodologies, data quality, and assumptions. Apart from the systematics and limitations of the pulsation models, the errors in derived parameters can also come from sparsely sampled observational light curves. More detailed investigations are needed in the methodologies for deriving stellar parameters based on light curve characteristics that can provide better constraints for the predictions of stellar pulsation and evolution models.

6 SUMMARY

This study on the M3 globular cluster encompassed various aspects to gain insights into the pulsation properties of its RR Lyrae population. We utilized a large photometric data set spanning 35 yr to obtain light curves of RR Lyrae stars at multiple filter bands. We recovered 238 previously known RR Lyrae stars in the M3 globular cluster, including 178 RRab stars, 49 RRc stars, and 11 RRd stars. Applying the MBLS algorithm (VanderPlas & Ivezić 2015) to our long-term photometric time-series data improved the accuracy and precision of the periods of 154 stars. To obtain accurate measurements of mean magnitudes and amplitudes from light curves with limited phase coverage or containing erroneous data points, we utilized a template fitting at multiple wavelengths.

Multiband photometric data were used to investigate the observed topology of the instability strip on the CMDs. Most RR Lyrae stars in M3 fall between the predicted boundaries of the instability strip based on stellar pulsation models. We filtered out outlier stars present in the data set using optical-NIR CMDs. Stars that were outliers in over 75 per cent of the CMDs were rejected and not considered further. Bailey’s diagram enabled a separation between RRab and RRc stars and confirmation of their classification. We also studied the relation of luminosity amplitude ratios (relative to the V band) with the pulsation period. We observed a general agreement between the derived values of ratios in different bands and those reported in the literature. However, in contrast to the findings of Bhardwaj et al. (2020) for JHK_s bands, we did not observe distinct values for long-period RRab stars.

The PLRs for the I and R bands were derived for RRab and RRc stars. We also investigated the PW relations for RR Lyrae stars in optical as well as NIR bands. The slopes for the FU and FO mode relations were found within 10 and 15 per cent, respectively when compared with theoretically predicted PL-metallicity relations (Marconi et al. 2015), while a slight discrepancy is observed for the Global mode. Using a combined sample of RR Lyrae stars, we derived a distance modulus of $\mu = 15.04 \pm 0.19(\text{syst.}) \pm 0.04(\text{stats})$ mag using the metal-independent W_{BV} Wesenheit magnitude. Similarly, using metal-dependent W_{VI} Wesenheits were used to derive a distance modulus of $\mu = 15.03 \pm 0.17(\text{syst.}) \pm 0.04$ mag. These results are in agreement with the current literature on the distance to the M3 cluster.

We studied the light curve structure of RR Lyrae stars in M3 using the Fourier decomposition method. The Fourier phase parameter ϕ_{31} exhibits a linear relation with the period, consistent with previous findings. Moreover, average phase parameters increase with wavelength at a given period. Finally, we utilized an artificial neural network that was trained with 8000 newly generated V -band light curve models to determine the physical parameters of non-Blazhko RRab stars in M3. We then applied the neural network to the observed V -band light curves of RRab stars in M3, determining their physical parameters. For the non-Blazhko RRab stars, the average values of the physical parameters are $M = 0.605 \pm 0.009 M_{\odot}$, $\log(L/L_{\odot}) = 1.71 \pm 0.04(\text{stats})\text{dex}$, and $T_{\text{eff}} = 6571 \pm 83$ K. These physical parameter estimates are within the diverse range of limited measurements for M3 RR Lyrae stars in the literature (Cacciari et al. 2005; Marconi & Degl’Innocenti 2007; Valcarce & Catelan 2008). Determining stellar parameters accurately is a challenging task, and the empirical differences highlight the need to improve the accuracy of physical parameters. This can also be done by adopting a multiwavelength approach, where the neural network is trained on light curves in several filters. More advanced machine-learning methods, together with the multiwavelength data, will be explored in

future to determine accurate and precise physical parameters of RR Lyrae stars, gaining new insights into our understanding of stellar evolution and pulsation.

ACKNOWLEDGEMENTS

We are grateful to PB Stetson for generously sharing the optical light curves of RR Lyrae stars in M3 used in this study. The authors acknowledge the usage of the IUCAA HPC computing facility for numerical calculations (training ANN models). NK acknowledges the financial assistance from the Council of Scientific and Industrial Research, India (CSIR), New Delhi, India, as the Senior Research Fellowship (SRF) file no. 09/45(1651)/2019-EMR-I. AB acknowledges funding from the European Union’s Horizon 2020 research and innovation programme under the Marie Skłodowska-Curie grant agreement Number 886298. HPS acknowledges a grant from the Council of Scientific and Industrial Research (CSIR), New Delhi, India, file no. 03(1428)/18-EMR-II.

DATA AVAILABILITY

The complete tables are available through Vizier.

REFERENCES

- Bailey S. I., 1902, *AnHar*, 38, 1
 Beaton R. L. et al., 2016, *ApJ*, 832, 210
 Bellinger E. P., Angelou G. C., Hekker S., Basu S., Ball W. H., Guggenberger E., 2016, *ApJ*, 830, 31
 Bellinger E. P., Kanbur S. M., Bhardwaj A., Marconi M., 2020, *MNRAS*, 491, 4752
 Benkő J. M., Szabó R., Paparó M., 2011, *MNRAS*, 417, 974
 Benkő J. M., Bakos G. A., Nuspl J., 2006, *MNRAS*, 372, 1657
 Bergstra J., Bengio Y., 2012, *J. Mac. Learn. Res.*, 13, 281
 Bhardwaj A., 2020, *JA&A*, 41, 23
 Bhardwaj A., 2022, *Universe*, 8, 122
 Bhardwaj A., Kanbur S. M., Singh H. P., Macri L. M., Ngeow C.-C., 2015, *MNRAS*, 447, 3342
 Bhardwaj A., Kanbur S. M., Marconi M., Rejkuba M., Singh H. P., Ngeow C.-C., 2017, *MNRAS*, 466, 2805
 Bhardwaj A., Rejkuba M., de Grijs R., Herczeg G. J., Singh H. P., Kanbur S., Ngeow C.-C., 2020, *AJ*, 160, 220
 Bhardwaj A. et al., 2021, *ApJ*, 909, 200
 Bhardwaj A. et al., 2023, *ApJ*, 944, L51
 Blazhko S., 1907, *Astron. Nachr.*, 175, 325
 Bono G., Caputo F., Castellani V., Marconi M., Storm J., 2001, *MNRAS*, 326, 1183
 Braga V. F. et al., 2015, *ApJ*, 799, 165
 Braga V. F. et al., 2016, *AJ*, 152, 170
 Cacciari C., Corwin T. M., Carney B. W., 2005, *AJ*, 129, 267
 Caputo F., 1990, *A&A*, 239, 137
 Castellani V., Quarta M. L., 1987, *A&AS*, 71, 1
 Castellani M., Castellani V., Cassisi S., 2005, *A&A*, 437, 1017
 Catelan M., 2004a, in Kurtz D. W., Pollard K. R., eds, *ASP Conf. Ser. Vol. 310, IAU Colloq. 193: Variable Stars in the Local Group*. Astron. Soc. Pac., San Francisco, p. 113
 Catelan M., 2004b, *ApJ*, 600, 409
 Catelan M., 2009, *Ap&SS*, 320, 261
 Catelan M., Pritzl B. J., Smith H. A., 2004, *ApJS*, 154, 633
 Clement C. M. et al., 2001, *AJ*, 122, 2587
 Clementini G., Gratton R., Bragaglia A., Carretta E., Di Fabrizio L., Maio M., 2003, *AJ*, 125, 1309
 Cohen J. G., Meléndez J., 2005, *AJ*, 129, 303
 Coppola G. et al., 2015, *ApJ*, 814, 71
 Corwin T. M., Carney B. W., 2001, *AJ*, 122, 3183

- Cox A. N., Hodson S. W., Clancy S. P., 1983, *ApJ*, 266, 94
- Cybenko G., 1989, *Math. Control Signals Syst.*, 2, 303
- Das S., Bhardwaj A., Kanbur S. M., Singh H. P., Marconi M., 2018, *MNRAS*, 481, 2000
- De Somma G., Marconi M., Molinaro R., Cignoni M., Musella I., Ripepi V., 2020, *AJ Suppl. Ser.*, 247, 30
- De Somma G., Marconi M., Molinaro R., Ripepi V., Leccia S., Musella I., 2022, *ApJS*, 262, 25
- Deb S., Singh H. P., 2009, *A&A*, 507, 1729
- Deb S., Singh H. P., 2010, *MNRAS*, 402, 691
- Denissenkov P. A., VandenBerg D. A., Kopacki G., Ferguson J. W., 2017, *ApJ*, 849, 159
- Di Criscienzo M., Marconi M., Caputo F., 2004, *ApJ*, 612, 1092
- Di Criscienzo M. et al., 2011, *AJ*, 141, 81
- Fabrizio M. et al., 2019, *ApJ*, 882, 169
- Fadeyev Y. A., 2019, *Astron. Lett.*, 45, 353
- Givens R. A., Pilachowski C. A., 2016, *PASP*, 128, 124203
- Harris W. E., 1996, *AJ*, 112, 1487
- Harris W. E., 2010, preprint (arXiv:1012.3224)
- Hartman J. D., Kaluzny J., Szentgyorgyi A., Stanek K. Z., 2005, *AJ*, 129, 1596
- Hornik K., 1991, *Neural Netw.*, 4, 251
- Hornik K., Stinchcombe M., White H., 1989, *Neural Netw.*, 2, 359
- Iben I. J., Huchra J., 1971, *A&A*, 14, 293
- Inno L. et al., 2015, *A&A*, 576, A30
- Johnson C. I., Kraft R. P., Pilachowski C. A., Sneden C., Ivans I. I., Benman G., 2005, *PASP*, 117, 1308
- Jones R. V., Carney B. W., Fulbright J. P., 1996, *PASP*, 108, 877
- Jurcsik J., 2019, *MNRAS*, 490, 80
- Jurcsik J., Kovács G., 1996, *A&A*, 312, 111
- Jurcsik J. et al., 2012, *MNRAS*, 419, 2173
- Jurcsik J. et al., 2015, *ApJS*, 219, 25
- Jurcsik J. et al., 2017, *MNRAS*, 468, 1317
- Jurcsik J., Hajdu G., Dékány I., Nuspl J., Catelan M., Grebel E. K., 2018, *MNRAS*, 475, 4208
- Kaluzny J., Kubiak M., Szymanski M., Udalski A., Krzemiński W., Mateo M., 1997, *A&AS*, 125, 343
- Kingma D. P., Ba J., 2014, preprint (arXiv:1412.6980)
- Kovacs G., Kanbur S. M., 1998, *MNRAS*, 295, 834
- Kovacs G., Zsoldos E., 1995, *A&A*, 293, L57
- Kovács G., Jurcsik J., 1996, *ApJ*, 466, L17
- Kumar N., Bhardwaj A., Singh H. P., Das S., Marconi M., Kanbur S. M., Prugniel P., 2023, *MNRAS*, 522, 1504
- Kunder A. et al., 2013, *AJ*, 146, 119
- Kunder A. et al., 2018, *SSRv*, 214, 90
- Landolt A. U., 1992, *AJ*, 104, 340
- Lee J.-W., Sneden C., 2021, *ApJ*, 909, 167
- Lenz P., Breger M., 2005, *Commun. Asteroseis.*, 146, 53
- Li L.-J., Qian S.-B., Zhu L.-Y., 2018, *ApJ*, 863, 151
- Lomb N. R., 1976, *Astrophys. Space Sci.*, 39, 447
- Longmore A. J., Fernley J. A., Jameson R. F., 1986, *MNRAS*, 220, 279
- Longmore A. J., Dixon R., Skillen I., Jameson R. F., Fernley J. A., 1990, *MNRAS*, 247, 684
- Madore B. F., 1982, *ApJ*, 253, 575
- Marconi M., Degl'Innocenti S., 2007, *A&A*, 474, 557
- Marconi M., Caputo F., Di Criscienzo M., Castellani M., 2003, *ApJ*, 596, 299
- Marconi M. et al., 2015, *ApJ*, 808, 50
- Molnár L. et al., 2021, *ApJS*, 258, 8
- Mullen J. P. et al., 2023, *ApJ*, 945, 83
- Muraveva T. et al., 2015, *ApJ*, 807, 127
- Neeley J. R. et al., 2019, *MNRAS*, 490, 4254
- Nemec J. M. et al., 2011, *MNRAS*, 417, 1022
- O'Malley T., Bursztein E., Long J., Chollet F., Jin H., Invernizzi L., 2019, KerasTuner. Available at: <https://github.com/keras-team/keras-tuner>
- Oosterhoff P. T., 1939, *The Observatory*, 62, 104
- Paxton B., Bildsten L., Dotter A., Herwig F., Lesaffre P., Timmes F., 2011, *ApJS*, 192, 3
- Paxton B. et al., 2013, *ApJS*, 208, 4
- Paxton B. et al., 2015, *ApJS*, 220, 15
- Paxton B. et al., 2018, *ApJS*, 234, 34
- Paxton B. et al., 2019, *ApJS*, 243, 10
- Pritzl B. J., Smith H. A., Catelan M., Sweigart A. V., 2001, *AJ*, 122, 2600
- Pritzl B. J., Smith H. A., Catelan M., Sweigart A. V., 2002, *AJ*, 124, 949
- Rood R. T., 1973, *ApJ*, 184, 815
- Savino A., Koch A., Prudil Z., Kunder A., Smolec R., 2020, *A&A*, 641, A96
- Scargle J. D., 1982, *ApJ*, 263, 835
- Schlegel D. J., Finkbeiner D. P., Davis M., 1998, *ApJ*, 500, 525
- Sesar B. et al., 2009, *ApJ*, 708, 717
- Shapley H., 1916, *ApJ*, 43, 217
- Siegel M. H., Porterfield B. L., Balzer B. G., Hagen L. M. Z., 2015, *AJ*, 150, 129
- Simon N. R., Clement C. M., 1993, *ApJ*, 410, 526
- Smolec R., Moskalik P., 2008, *Acta Astron.*, 58, 193
- Sneden C., Kraft R. P., Guhathakurta P., Peterson R. C., Fulbright J. P., 2004, *AJ*, 127, 2162
- Sollima A., Cacciari C., Valenti E., 2006, *MNRAS*, 372, 1675
- Soszyński I., Gieren W., Pietrzyński G., 2005, *PASP*, 117, 823
- Stetson P. B., 1987, *PASP*, 99, 191
- Stetson P. B., 1994, *PASP*, 106, 250
- Stetson P. B. et al., 2014a, *PASP*, 126, 521
- Stetson P. B., Fiorentino G., Bono G., Bernard E. J., Monelli M., Iannicola G., Gallart C., Ferraro I., 2014b, *PASP*, 126, 616
- Stetson P. B., Pancino E., Zocchi A., Sanna N., Monelli M., 2019, *MNRAS*, 485, 3042
- Szeidl B., Hurta Z., Jurcsik J., Clement C., Lovas M., 2011, *MNRAS*, 411, 1744
- Valcarce A. A. R., Catelan M., 2008, *A&A*, 487, 185
- VandenBerg D. A., Denissenkov P. A., Catelan M., 2016, *ApJ*, 827, 2
- VanderPlas J. T., Ivezić V., 2015, *ApJ*, 812, 18
- Wallerstein G., Kovtyukh V. V., Andrievsky S. M., 2009, *ApJ*, 692, L127

SUPPORTING INFORMATION

Supplementary data are available at *MNRAS* online.

suppl.data

Please note: Oxford University Press is not responsible for the content or functionality of any supporting materials supplied by the authors. Any queries (other than missing material) should be directed to the corresponding author for the article.

APPENDIX A: TRAINING OF ANN

We used the architecture outlined in Table A1 to build the *RRab-Net* for the *V* band. This architecture selection followed a Grid search for hyperparameters, as explained in Section 5.2. It is essential to note that high learning rates can induce oscillations in the learning curve, which can be reduced by lowering the learning parameter. However, starting training with a low η can negatively impact network performance. To address this, we used a ‘piece-wise decay’

Table A1. The adopted network architecture of the *RRab-Net* after hyperparameter optimization using a random search algorithm.

S. N.	Name of hyperparameter	Value
1	Number of hidden layers	3
2	No of neurons in hidden layers	[128, 64, 64]
3	Optimizer	‘adam’ (Kingma & Ba 2014)
4	Learning rate	6.7984×10^{-4} (decreasing with number of epochs)
5	Activation function	‘tanh’
6	Weights initialization	‘GlorotUniform’

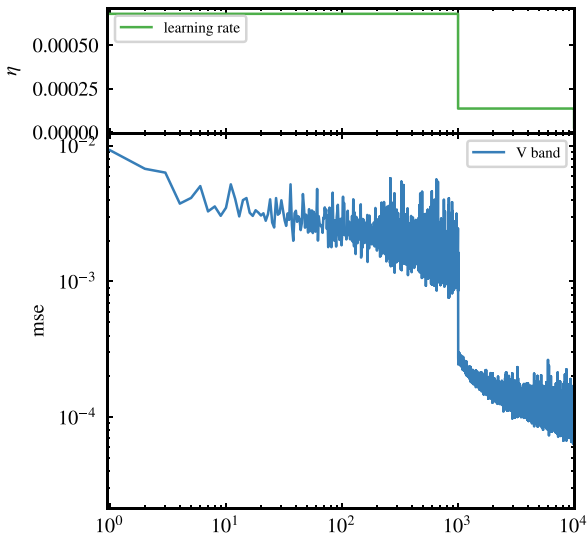


Figure A1. The training curves for V band *RRab-Net*.

approach, where the current learning rate is divided by a constant number (δ) when the epoch crosses successive powers of 10. After experimenting with different values, we chose $\delta = 5$. This ensures that the loss decreases gradually as training progresses. We trained the network for 10 000 epochs and achieved a minimum MSE of 3.02×10^{-5} . The final learning curve and learning parameter (η) are shown in Fig. A1.

APPENDIX B: ADDITIONAL TEMPLATE FIT LIGHT CURVES

We present two additional figures showcasing the light curves of RR Lyrae stars in different filter bands. Fig. B1 displays the light curves of the non-Blazhko RRab star V31 (left-hand panel) and the Blazhko RRab star V48 (right-hand panel). The period of V31 is 0.580727 d, while V48 exhibits a primary period of 0.627830 d. Similarly, Fig. B2 illustrates the light curves of the non-Blazhko RRc star V75 (left-hand panel) and the Blazhko RRc star V140 (right-hand panel). The period of V75 is 0.314078 d, whereas V140 demonstrates a primary period of 0.333139 d. Both figures follow the same nomenclature as depicted in Fig. B1 for clarity and consistency.

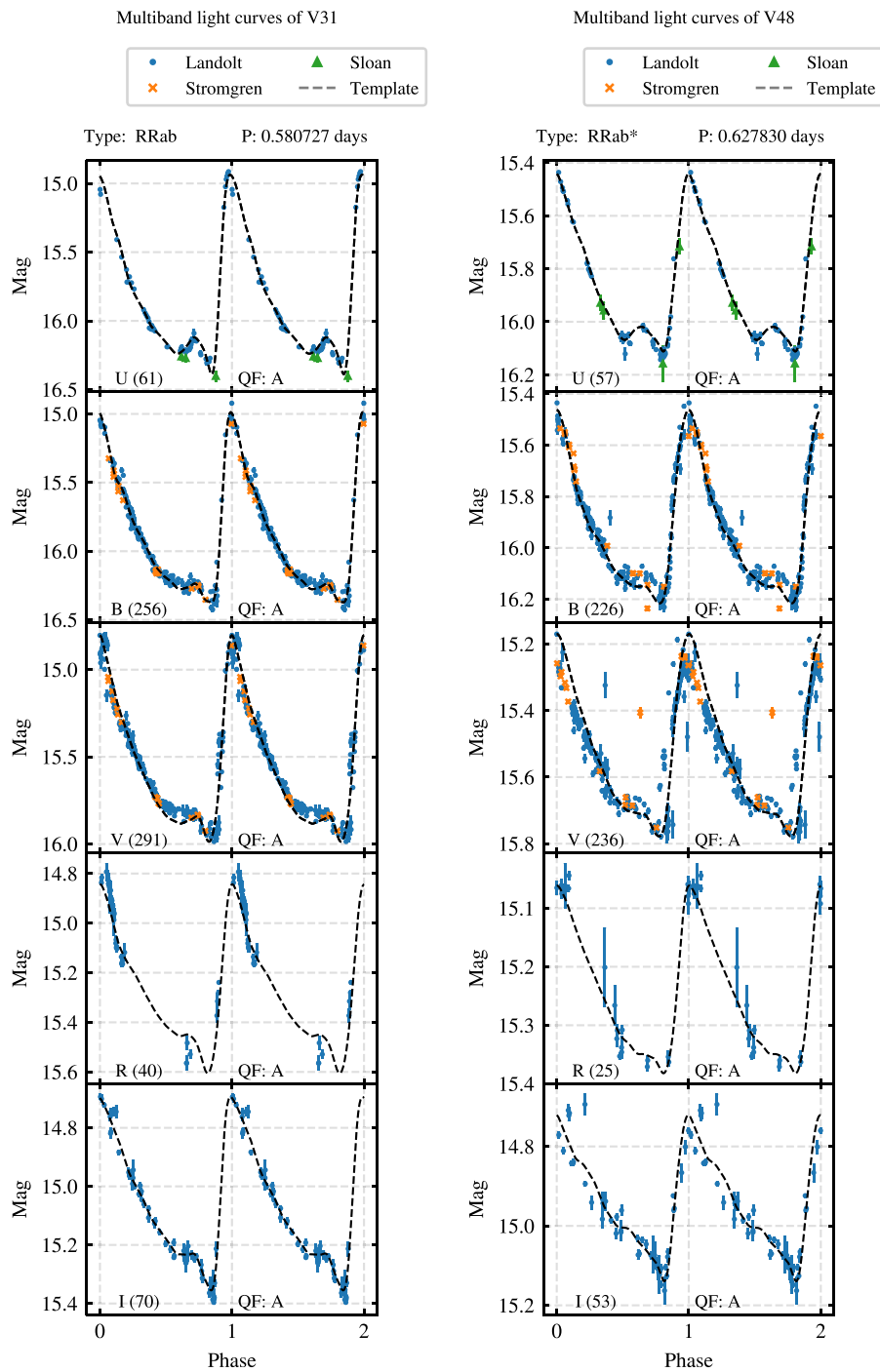


Figure B1. The left-hand panel presents the *U*, *B*, *V*, *R*, and *I* band light curves of the V31 (non-Blazhko RRAb) star. The period of this star is 0.580727 d. The folded light curves of the Blazhko RRAb star V48 are displayed in the right-hand panel, with a primary period of 0.627830 d. The adopted nomenclature for this figure is same as Fig. 4.

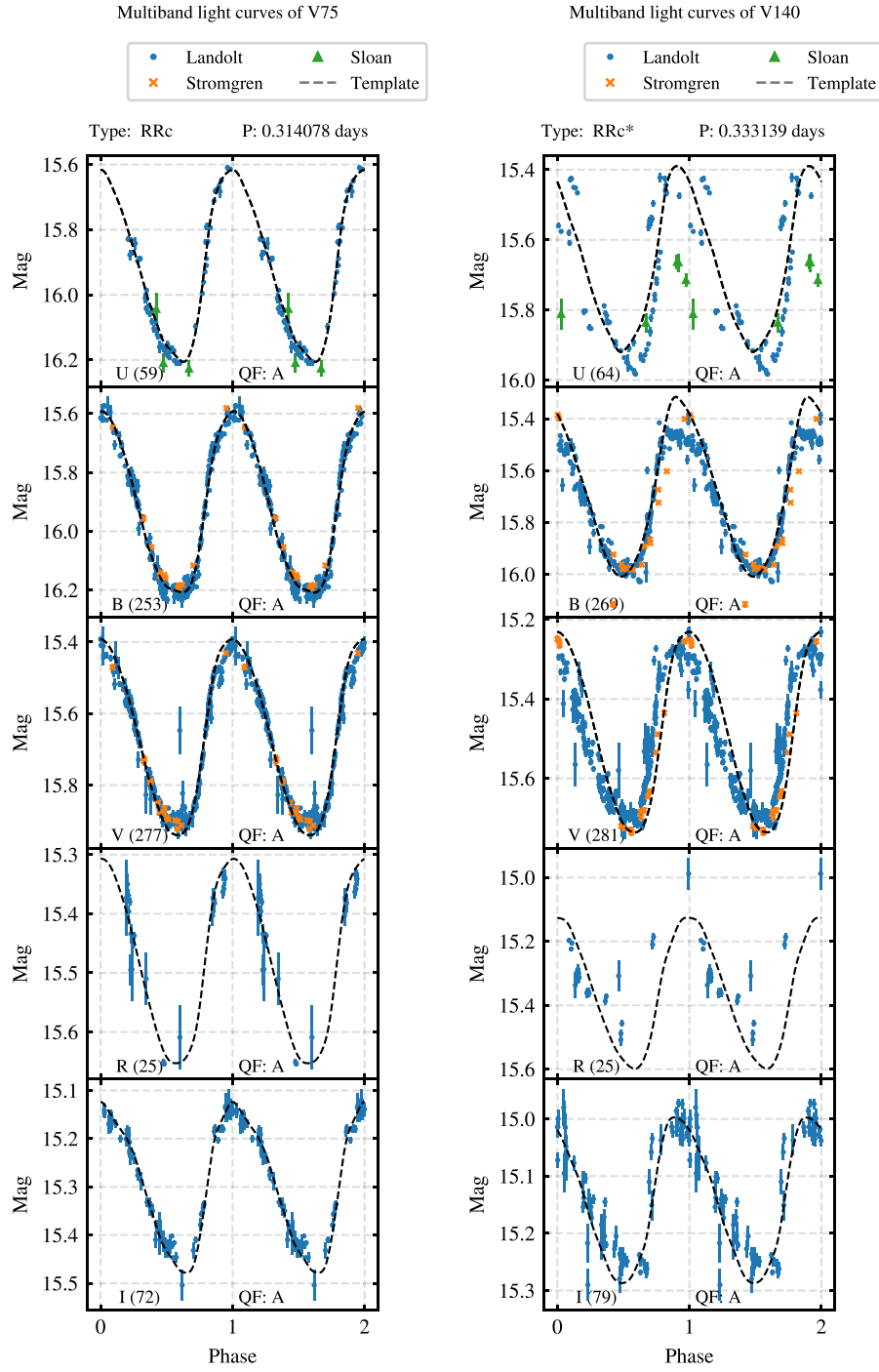


Figure B2. The left-hand panel presents the *U*, *B*, *V*, *R*, and *I* band light curves of the V75 (non-Blazhko RRc) star. The period of this star is 0.314078 d. The folded light curves of the Blazhko RRc star V140 are displayed in the right-hand panel, with a primary period of 0.333139 d. The adopted nomenclature for this figure is same as Fig. 4.

This paper has been typeset from a $\text{\TeX}/\text{\LaTeX}$ file prepared by the author.